Spray Combustion Simulation of a Single-Element LOX/H_2 Rocket Combustor

Sprayverbrennungssimulation einer Single-Element LOX/H_2 Raketenbrennkammer

Nikolaos Perakis

Semesterarbeit
Luft- und Raumfahrt
Technische Universität München

Betreuer: Dipl.-Ing. Christof Roth
Prof. Oskar J. Haidn
Abgabe: März 31, 2016

Lehrstuhl für Flugantriebe, LFA
Fachgebiet Raumfahrtantriebe

2016

Aknowledgements

I would like to thank my supervisor Dipl.-Ing. Christof Roth for his constant support throughout the 5 months of the thesis. I really appreciate the time he invested in the project and the interest he demonstrated during our discussions, always eager to share his advice and try to tackle the issues I encountered.

I would also like to thank Prof. Oskar J. Haidn for allowing me to carry out my thesis within the Department of Flight Propulsion and all colleagues at the department for their ideas and comments.

Munich, March 31 2016

Nikolaos Perakis

Contents

Symbols and Abbreviations

Symbols

A_o	Arrhenius constant $\left[\mathrm{s}^{-1}\right]$
$[A]$	Species concentration $\left[\mathrm{mol/m}^3\right]$
A_p	Particle surface area $\left[\mathrm{m}^2\right]$
A_t	Throat cross sectional area $\left[\mathrm{m}^2\right]$
B_m	Spalding mass number [−]
c	Speed of light [m/s]
c_p	Specific heat capacity $[\mathrm{J/(kg \cdot K)}]$
C_d	Drag coefficient [−]
d	Diameter [m]
d_{max}	Rosin-Rammler maximal diameter [m]
d_{min}	Rosin-Rammler minimal diameter [m]
d_{ref}	Rosin-Rammler size constant [m]
d_p	Particle diameter [m]
D	Mass diffusion coefficient $\left[\mathrm{m}^2/\mathrm{s}\right]$
D_i	Injector diameter [m]
D_t	Turbulent mass diffusion coefficient $\left[\mathrm{m}^2/\mathrm{s}\right]$
E_a	Activation energy [J/mol]
f	Mass probability density function [−]
$\vec{F}$	Force [N]
$\vec{F}_w$	Drag force [N]
G	Incident radiation $\left[\mathrm{W/m}^2\right]$
h	Convection coefficient $\left[\mathrm{W/(m}^2 \cdot \mathrm{K)}\right]$
h_P	Planck constant $\left[\mathrm{m}^2/(\mathrm{kg \cdot s})\right]$
H	Enthalpy [J/kg]
J	Momentum flux ratio [−]
k	Turbulent kinetic energy [J/kg]
k_B	Boltzmann constant [J/K]

k_r	Reaction rate $\left[\mathrm{mol}/(\mathrm{m}^3 \cdot \mathrm{s})\right]$
l^*	Characteristic chamber length [m]
m_p	Particle mass [kg]
$\dot{m}$	Mass flow rate [kg/s]
$\dot{m}_p$	Mass rate of evaporation [kg/s]
M	Molecular weight [kg/mol]
n	Rosin-Rammler size parameter [−]
N	Number of droplets [−]
N_A	Avogadro number $\left[\mathrm{mol}^{-1}\right]$
OF	Oxidizer to fuel ratio [−]
p	Pressure [bar]
p_c	Critical pressure [bar]
p_r	Reduced pressure [−]
p_{sat}	Saturation pressure [bar]
P	Probability density function [−]
Pr	Prandtl number [−]
Pr_t	Turbulent Prandtl number [−]
R	Universal gas constant $[\mathrm{J}/(\mathrm{mol} \cdot \mathrm{K})]$
Re	Reynolds number [−]
Re_p	Relative particle Reynolds number [−]
S	Source term $\left[\mathrm{kg}/(\mathrm{m}^3 \cdot \mathrm{s})\right]$
Sc	Schmidt number [−]
Sc_t	Turbulent Schmidt number [−]
t	Time [s]
T	Temperature [K]
T_c	Critical temperature [K]
T_r	Reduced temperature [−]
T_p	Particle temperature [K]
T_∞	Continuous phase temperature [K]
T_b	Boiling temperature [K]
T_{ev}	Evaporation temperature [K]
$\vec{v}$	Velocity [m/s]
$\bar{v}$	Mean velocity [m/s]
v'	Velocity fluctuation [m/s]

$\vec{v}_p$	Particle velocity [m/s]
V_c	Combustion chamber volume $\left[\mathrm{m}^3\right]$
We	Webber number [−]
Y	Species mass fraction [−]
Z	Mixture fraction [−]
$\bar{Z}$	Mean mixture fraction [−]
Z'	Mixture fraction variance [−]
α	Beta function coefficient [−]
β	Beta function coefficient [−]
Δg^0	Gibbs enthalpy of formation [J/mol]
Δh_{ev}	Enthalpy of evaporation [J/kg]
ϵ	Turbulent dissipation rate $[\mathrm{J}/(\mathrm{kg}\cdot\mathrm{s})]$
ϵ_c	Chamber contraction ratio [−]
ϵ_p	Particle emissivity [−]
θ	Angle [deg]
κ	Arrhenius exponent [−]
λ	Heat conductivity $[\mathrm{W}/(\mathrm{m}\cdot\mathrm{K})]$
λ_{OH}	Emitted wavelength from OH radicals [m]
μ	Viscosity $[\mathrm{kg}/(\mathrm{m}\cdot\mathrm{s})]$
μ_t	Turbulent viscosity $[\mathrm{kg}/(\mathrm{m}\cdot\mathrm{s})]$
ν	Stoichiometric coefficient [−]
ρ	Density $\left[\mathrm{kg}/\mathrm{m}^3\right]$
ρ_p	Particle density $\left[\mathrm{kg}/\mathrm{m}^3\right]$
σ	Surface tension [N/m]
σ_C	Average collision diameter [Å]
σ_S	Stefan-Boltzmann constant $\left[\mathrm{W}/(\mathrm{m}^2\cdot\mathrm{K}^4)\right]$
σ_{st}	Standard deviation [m]
ϕ	Dependent quantity [arbitrary]
Ψ	Cumulative density function [−]
Ω	Collision integral [−]

Abbreviations

2D, 3D	two, three dimensions / -dimensional
CCD	Charged Coupled Device
CARS	Coherent anti-Stokes Raman Spectroscopy
CFD	Computational Fluid Dynamics
CNES	Centre National d'Études Spatiales
CNRS	Centre National de la Recherche Scientifique
DNS	Direct Numerical Simulation
DP	Discrete Phase
DRW	Discrete Random Walk
GH_2	Gaseous hydrogen
LH_2	Liquid hydrogen
LOX	Liquid oxygen
NIST	National Institute of Standards and Technology
ONERA	Office National d'Etudes et de Recherches Aérospatiales
PDF	Probability Density Function
PPDF	Presumed Probability Density Function
RANS	Reynolds-Averaged Navier-Stokes
SSME	Space Shuttle Main Engine
TUM	Technische Universität München
UV	Ultraviolet

Abstract

The goal of this thesis is to simulate the cryogenic LOX/H_2 combustion of the single element Mascotte combustor in subcritical conditions. The simulation is carried out by using the Lagrange droplet tracking module implemented in the commercial CFD-Tool Fluent, with the purpose of validating the tool and exploring its modeling capabilities in the case of spray combustion calculations. The test case is simulated extensively on a two-dimensional, axially symmetric grid with the aim to reduce computational cost. For the validation of the numerical results, the hot gas temperature measurements as well as experimental OH^* emissions are utilized.

For the characterization of the droplets' initial diameters, a Rosin-Rammler distribution is implemented, as proposed by previous literature works which have examined the same test case. Several parameter studies are performed to produce results approximating the experimental data as close as possible. Specifically, the injection angle of the oxygen particles, their initial velocity magnitude as well as the turbulent Prandtl and Schmidt numbers are varied. Moreover, special emphasis is put on the comparison of different heat and mass transfer models for the discrete phase. Models involving surface evaporation, boiling, radiation as well as their combinations are examined and compared to each other. Finally the interaction of the droplets with the chamber walls is shortly discussed. The results of the numerical simulation after the comparison of the different boundary conditions and models lead to temperature profiles and OH^* emissions fitting the experimental data, serving as a validation of the Lagrange tracking module.

1. Introduction

The development of today's rocket engines relies heavily on the numerical simulation of the physical processes taking place within the rocket thrust chamber. Due to the costs associated with experimental testing programs, trial and error approaches have been limited by the rocket propulsion industry in the process of developing new propulsion systems [18]. The application of analytical tools and numerical simulations allow for a more resource efficient way of carrying out trade-off studies, understanding physical processes and optimizing the performance in the design process of propulsion systems.

Numerical simulations in the field of space propulsion are a powerful tool which enables predictions of the combustion and heat transfer phenomena taking place in the hot gas. However, the reliability of a simulation is imminently connected to the models which are being implemented and their validation. The complexity of the physical and chemical mechanisms taking place in a combustion chamber, involving atomization, evaporation, mixing, two phase flows, supercritical and real gas thermodynamics, chemical reactions, supersonic velocities and interaction of the flow with the structure, requires the implementation of models, which simplify some of the simulated processes. In the absence of models, the representation of all physical processes would render the simulation time-consuming and hence inefficient for designing purposes. In the procedure of implementing models into the simulation, the physical mechanisms with negligible influence on the final result have to be identified and omitted or simplified to reduce the computational cost. The knowledge of the introduced simplifications and used models is crucial for understanding the applicability limits of the simulation. Finally, the validation of the utilized models is necessary to ensure a reliable predictability. This occurs by comparing the simulation results with well established test cases.

Of specific interest are the applications involving liquid-propellant rocket engines, since those systems have been used as primary means of propulsion in most launch vehicles and spacecraft. The combination of hydrogen (H_2) and oxygen (O_2) has been widely used as a propellant in liquid rocket engines, in-

cluding the Space Shuttle Main Engine (SSME) and the Vulcain 2 engine of the European launcher Ariane. Due to hydrogen's very low molecular weight, a high specific impulse is produced, leading to advanced performance [34]. Due to its very low density , hydrogen is usually stored under cryogenic conditions in liquid phase. However, hydrogen can also be used as a cooling agent, flowing through the walls of the thrust chamber and absorbing high heat fluxes before being injected into the combustion chamber in the case of regenerative cooling cycles [26]. This way hydrogen enters the chamber in gaseous form (GH_2). In the majority of space applications, oxidizer and fuel are injected through coaxial injectors, with the gaseous hydrogen surrounding the central jet of liquid oxygen (LOX).

Figure 1.1 illustrates this concept based on the example of the Vulcain 2 engine. LH_2 exits the pump (which is driven by a gas generator) and flows along the nozzle wall before being injected into the chamber in gaseous form with the LOX. The injection plate of the Vulcain 2 LRE, composed of 566 coaxial injectors is shown in Figure 1.2.

A physical process with significant influence on the behavior and performance of the injector and extensively the liquid rocket engine is the one of vaporization and combustion of a liquid oxidizer in the presence of the gaseous fuel. Therefore the modeling and simulation of this spray-combustion mechanism is the focus of the present thesis. The tracking of the liquid particles and their vaporization is examined for the case of a LOX/H_2 combustor. The so-called Lagrange tracking module provided by the commercial solver ANSYS Fluent is examined for its capability of simulating the physical processes taking place in a rocket combustion chamber. This module enables tracking the liquid phase as individual droplets which interact with the gas phase until they evaporate or escape the domain.

For the validation of the model, the experimental measurements of the Mascotte test case A-10 [35] of the French national aerospace research center ONERA were used. The optically accessible chamber provides temperature and OH^*-emission measurements which can be directly compared to the obtained numerical results. This single-element LOX/H_2 chamber uses a coaxial injector and the A-10 test case has an operating pressure of 10 bar, leading to subcritical conditions for both the fuel and the oxidizer.

In Chapter 2 a short introduction to the theory of the chemistry modeling

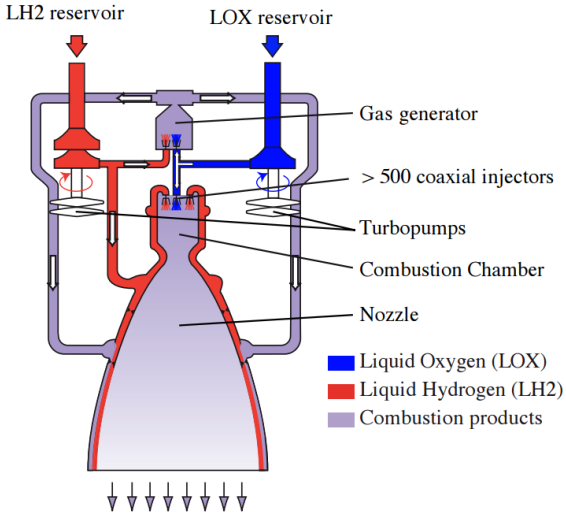

Figure 1.1.: Operating principle of the Vulcain 2 engine [31]

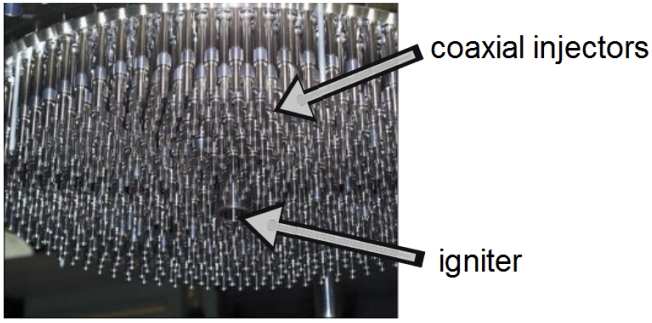

Figure 1.2.: Injection plate of the Vulcain 2 LRE [2]

and to the Lagrange tracking module is given, before describing the specifics of the A-10 Mascotte case, which is examined in this thesis, in Chapter 3. The analysis of the simulation's settings as well as the numerical results are presented in Chapter 4. Here, several parameter analyses and comparisons are carried out, to ensure that the final result captures the physics of the LOX evaporation and subsequent O_2/H_2 combustion sufficiently. Finally, Chapter 5 gives a short summary of the implemented methods and the Lagrange tracking module's capabilities and discusses further steps that can potentially improve the results.

2. Theory and Modeling

The simulation of the two-phase flow occurring in the coaxial injector of the Mascotte A-10 case is carried out with a separation between the liquid and the gaseous phase. The gaseous phase is modeled according to the Euler formulation of the Navier-Stokes equations, whereas a Lagrange module is implemented for the liquid oxygen. The calculation is implemented in a two-dimensional (2D) axisymmetric computational domain with the use of the commercial tool ANSYS Fluent [1].

2.1. Modeling of gas phase

The simulation of the gas phase flow was carried out with the use of the Raynolds-Averaged Navier-Stokes (RANS) equations. The solved equations for continuity, impulse and energy are not discussed within the frame of this thesis since their theory has been extensively analyzed in the literature [12]. The closure of the Reynolds stress tensor was done with the use of the RANS-k-ϵ model for the turbulence modeling [36].

In the case of rocket engine simulations, an important factor which directly influences the performance of the engine, since it defines the energy release and temperature distribution, lies in the used combustion model. For the validation of the Lagrange module, where the evaporation of the particles is dictated by the temperature field in the chamber, the use of a realistic combustion model is crucial since it directly affects the amount of oxidizer which evaporates upon interaction with the hot gas.

The modeling of the chemical reactions can be undertaken with a global chemistry mechanism, which calculates the rate constant k_r at the temperature T according to the Arrhenius law [28]

$$k_r = A_o T^{\kappa} \cdot e^{-\frac{E_a}{RT}} \tag{2.1}$$

where A_o stands for the Arrhenius constant, E_a the activation energy that

has to be overcome for the reaction to take place and R for the universal gas constant. Assuming a generic chemical reaction of the form

$$\nu_1 A + \nu_2 B \rightleftharpoons \nu_3 C + \nu_4 D \tag{2.2}$$

with ν_i representing the stoichiometric coefficients, the reaction rate r_f and r_b for the forward and backward reactions are given by

$$r_f = k_{r,f} \left[A\right]^{\nu_1} \left[B\right]^{\nu_2} \text{ and } r_b = k_{r,b} \left[C\right]^{\nu_3} \left[D\right]^{\nu_4} \tag{2.3}$$

The use of the finite rate chemistry model requires the solution of $N-1$ additional conservation equations for the N species being modeled in the simulation and can therefore become computationally expensive.

In the case of hydrogen combustion, the kinetic rates k_r take very high values, leading to very fast characteristic chemical time scales. For that reason, the assumption of chemical equilibrium can be made. Under this assumption, the forward and backward reaction rates for the reactants and products are equal or else

$$r_f = r_b \tag{2.4}$$

The properties of the chemical equilibrium including temperature and gas compositions can be calculated by the condition that the Gibb's free enthalpy demonstrates a minimum [3], [15].

When dealing with chemical equilibrium combustion modeling, the introduction of the mean mixture fraction Z is helpful. It is defined as the mass fraction of the fuel stream in the mixture [27] according to Eq. 2.5:

$$Z = \frac{\dot{m}_f}{\dot{m}_f + \dot{m}_{ox}} = \frac{1}{1+OF} \tag{2.5}$$

In this definition $\dot{m}_f$ and $\dot{m}_{ox}$ stand for the mass flows of fuel and oxidizer respectively and OF for the oxidizer to fuel ratio.

Under the assumption of equal diffusivities, the species equations can be reduced to a single conservation equation for the mixture fraction Z. For the mean density-averaged mixture fraction $\bar{Z}$, the equation yields for the stationary case:

$$\nabla \cdot (\rho \vec{v} \bar{Z}) = \nabla \cdot \left(\frac{\mu_t}{Sc_t} \nabla \bar{Z} \right) + S_{evap,Z} \tag{2.6}$$

In Eq. 2.6, ρ represents the density, $\vec{v}$ the velocity vector, μ_t the turbulent viscosity, Sc_t the turbulent Schmidt number and $S_{evap,Z}$ the source term representing the transfer of mass into the gas phase from the liquid droplets [1].

The condition that $Z = \bar{Z}$ is only valid when no turbulence effects are included in the simulation. In the case where the flow is not laminar, the instantaneous values of Z have to be connected with the mean value $\bar{Z}$ according to a turbulence-chemistry interaction model. This is enabled by solving a conservation equation for the mixture fraction variance $Z' = Z - \bar{Z}$, which is given by Eq. 2.7 [16].

$$\nabla \cdot (\rho \vec{v} Z'^2) = \nabla \cdot \left(\frac{\mu_t}{Sc_t} \nabla Z'^2 \right) + C_g \mu_t \left(\nabla Z' \right)^2 - 2\rho \frac{\epsilon}{k} Z'^2 \tag{2.7}$$

where C_g is an empirical constant equal to 2.86, ϵ is the turbulent dissipation rate and k the turbulent kinetic energy.

Upon knowledge of the mixture fraction Z and the exchanged enthalpy H for the non-adiabatic case, where radiation, heat transfer through walls, and heat exchange with the Discrete Phase (DP) droplets is allowed, the instantaneous values for the independent quantities ϕ, i.e. mass fraction, density and temperature can be obtained. In the case of adiabatic systems, the knowledge of Z is sufficient to determine all these instantaneous values. These instantaneous, fluctuating fields are connected to the averaged values $\bar{\phi}$ by applying a Presumed Probability Density Function (PPDF) as a closure for the combustion model. The PPDF $P(Z)$ can be thought of as the fraction of time that the fluid spends in the vicinity of the state Z. This yields for $\bar{\phi}$ [14]:

$$\bar{\phi} = \int_0^1 \phi(Z, \bar{H}) P(Z) \mathrm{d}Z \tag{2.8}$$

for a given value of the exchange enthalpy $\bar{H}$. In order to reduce the computational time, the integral of Eq. 2.8 are carried out only once and stored in a look-up table, which contains information for the averaged scalar values $\bar{\phi}$ as a function of $\bar{Z}$, Z' and $\bar{H}$. This is also the main advantage of using the equilibrium model compared to a global mechanism, since the tabulation significantly

speeds up the calculations.

The common choice for the PPDF $P(Z)$ is the so-called Beta-Function [14]. This is defined as in Eq. 2.9

$$P(Z) = \frac{Z^{\alpha-1}(1-Z)^{\beta-1}}{\int Z^{\alpha-1}(1-Z)^{\beta-1}\mathrm{d}Z} \tag{2.9}$$

with

$$\alpha = \bar{Z}\left[\frac{\bar{Z}(1-\bar{Z})}{Z'^2} - 1\right]$$

and

$$\beta = \frac{1-\bar{Z}}{\bar{Z}}\alpha$$

2.2. Modeling of Discrete Phase (DP)

2.2.1. Liquid jet break-up

In the case of coaxial injectors, the liquid core is introduced into the chamber through a tube and is surrounded by a co-flowing gaseous fuel. The physical processes that the liquid jet is subject to, when entering the chamber, are divided into the following categories:

1. Injection [4]
2. Atomization [23]
3. Particle transport and turbulent dispersion [33]
4. Droplet/droplet and droplet/wall interaction [32]
5. Evaporation [19]

Directly after the injection, the interaction of the liquid core with the surrounding gas flow leads to a shear between the two phases and creates surface instabilities. These shear flow instabilities lead to a break-up of the central core and the liquid's surface tension results in the formation of liquid sheets and ligaments, a process which is referred to as "primary atomization". The

viscosity and inertia of the liquid demonstrate a damping effect on the disintegration dynamics. The formation of ligaments and droplets is classified by the dimensionless Webber number We and the momentum flux ratio J:

$$We = \frac{\rho_f (v_f - v_{ox})^2 d_{ox}}{\sigma} \tag{2.10}$$

$$J = \frac{\rho_f v_f^2}{\rho_{ox} v_{ox}^2} \tag{2.11}$$

with ρ_f and ρ_{ox} representing the densities of fuel and oxidizer, v_f and v_{ox} their respective velocities, d_{ox} the oxidizer jet diameter and σ the fluid's surface tension [7], [20].

Further downstream of the injector, the interaction between ligaments and/or droplets, as well as the aerodynamic forces that the fluid is subject to (because of interaction with the gas phase) leads to a further break-up called "secondary atomization". These phenomena are illustrated schematically in Fig. 2.1.

The process of atomization remains a challenging topic of research, where DNS simulations provide a promising tool in realistically predicting the break-up of the initial liquid jet. The DNS simulation of a 3D liquid jet injection is illustrated in Fig. 2.2. The break-up of LOX jet into droplets is not part of the present thesis due to its complexity. For that reason, the liquid phase is initialized with a given droplet distribution after the injection, as explained in Section 2.2.2.

2.2.2. Initial particle distribution

The modeling of the liquid phase occurs with a Lagrange module, which simulates the liquid oxygen as discrete particles. Therefore, the processes of primary and secondary break-up are not modeled and the introduction of the liquid phase into the computational domain takes place as a group of droplets.

The size of the droplets is an important factor which directly influences their evaporation characteristics and hence impacts the interaction of the discrete phase with the gas flow. For the definition of the initial diameter of the particles, a continuous probability function is utilized. In the present simulation, the Rosin-Rammler diameter distribution model was implemented since it allows for a flexible representation of the size scattering. According to the model,

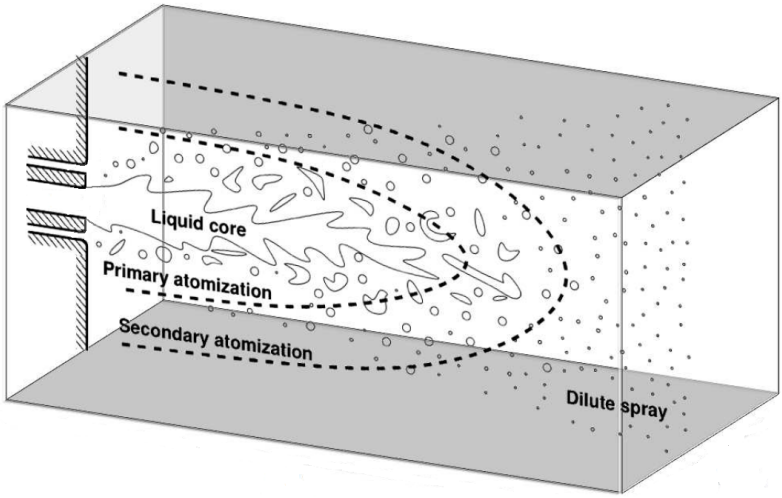

Figure 2.1.: Turbulent atomization of coaxial injector (modified from Desjardins et al. [11]

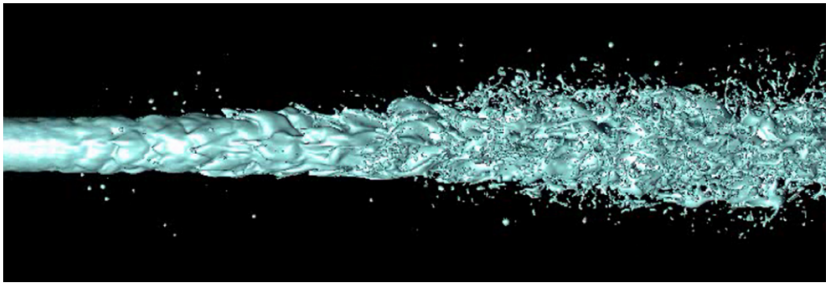

Figure 2.2.: Liquid jet surface and break-up results of DNS simulation [23]

the mass fraction of droplets with diameter greater than d (cumulative density function) is given by

$$\Psi(d) = e^{-(d/d_{ref})^n} \tag{2.12}$$

where d_{ref} is the size constant and n the size distribution parameter. This results in a mass probability density function for the particles equal to

$$f(d) = e^{-(d/d_{ref})^n} \frac{n}{d_{ref}} \left(\frac{d}{d_{ref}}\right)^n \tag{2.13}$$

The probability density function for several combinations of d_{ref} and n is shown in Fig. 2.3.

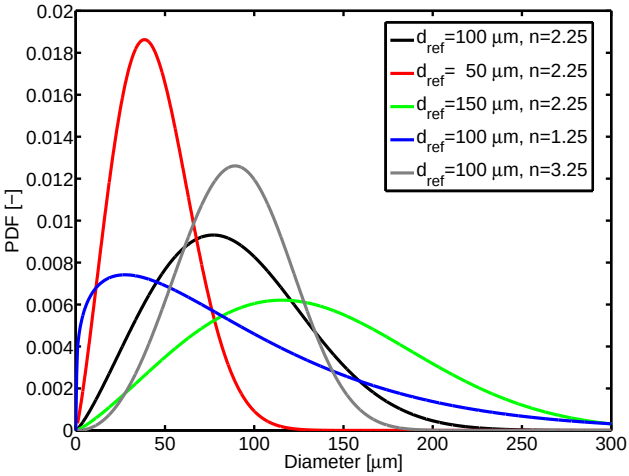

Figure 2.3.: Probability density function of Rosin-Rammler distribution for various parameters

Given a Rosin-Rammler distribution function and the total mass of the liquid particles m_{tot}, then the total number of droplets N with a specific diameter d_i can be calculated according to

$$N(d_i) = \frac{f(d_i) \cdot m_{tot}}{\frac{\pi}{6} d_i^3 \rho_i} \tag{2.14}$$

where ρ_i stands for the density of each droplet. The relative number of particles (normalized to the maximal value of 1) for different distribution parameters is shown in Fig. 2.4. It is therefore evident, that although the mass-based PDF has its maximum at higher diameters close to d_{ref}, the vast majority of particles modeled has a very small diameter close to 1 μm, which however contributes only to a small mass fraction of the total liquid phase (large number of particles but low total volume).

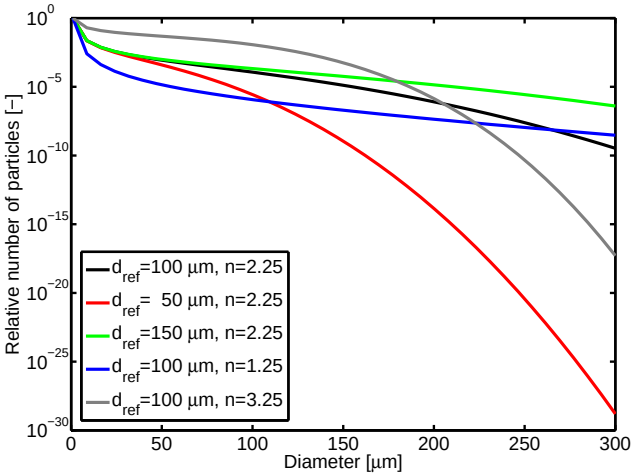

Figure 2.4.: Particle number according to the Rosin-Rammler distribution for various parameters

2.2.3. Lagrange particle transport

After the initial conditions of the droplet distribution have been established according to the PDF described in Section 2.2.2, the distinct particles are injected into the domain. In general, the description of the two-phase flow can be separated into three separate methods [8]

1. Continuous-Particle Models
2. Continuum-Formulation

3. Discrete-Particle Models

The first method employs a multidimensional distribution function that allows for a statistically accurate field description of the liquid spray. The continuum-formulation treats the gas and liquid phases as interpenetrating continua which are described in an Euler frame. In the case of the discrete-particle model, a finite number of particles is introduced into the domain and their trajectory is calculated by solving a set of Lagrangian equations of motion.

In the framework of this thesis, the built-in Lagrange tracking module of Fluent using the discrete particle model was implemented. Due to the large number of physical particles in the liquid stream and the computational effort their tracking would induce, a sampling is employed, according to which the properties of droplet groups are summarized and represented by computational parcels. This way, each parcel can represent many physical droplets and acts itself as a particle, which interacts with the bulk gas phase by exchanging momentum, mass and energy with it. A simplification of this approach is made when particle-particle interactions are neglected. This assumption is justifiable when the dispersed phase occupies a low volume fraction, smaller than 10 % [17]. According to this model, which was also used for the simulations presented here, each parcel is tracked individually until it escapes the domain through an outlet or evaporates completely.

The momentum equation for the individual parcels with mass m_p and velocity $\vec{v}_p$ takes the form of Newton's second law of motion and hence reads:

$$m_p \frac{\mathrm{d}\vec{v}_p}{\mathrm{d}t} = \sum_i \vec{F}_i \tag{2.15}$$

where $\vec{F}_i$ are the forces acting on the particle. The main contribution to the momentum equation comes from the drag force $\vec{F}_w$ which can be modeled as:

$$\vec{F}_w = \frac{3\mu C_d Re_p}{4\rho_p d_p^2} \cdot (\vec{v} - \vec{v}_p) \tag{2.16}$$

where μ, ρ and $\vec{v}$ represent the dynamic viscosity, density and velocity of the gas phase and ρ_p, d_p and $\vec{v}_p$ the density, diameter and velocity of the particle. Re_p is the relative Reynolds number defined as in Eq. 2.17.

$$Re_p = \frac{\rho d_p |\vec{v}_p - \vec{v}|}{\mu} \tag{2.17}$$

C_d stands for the drag coefficient experienced by the particle. For spherical particles, the drag law is expressed as a function of the gas Reynolds number according to Morsi and Alexander [24] and is given by Eq. 2.18.

$$C_d = a_0 + \frac{a_1}{Re} + \frac{a_2}{Re^2} \tag{2.18}$$

Non-spherical drag laws were not included in the modeling of the discrete phase and neither were sub-micron effects like the Stokes-Cunnigham drag law [25], since the majority of the particles has initial diameters well above this limit as seen in Section 4.2. Apart from aerodynamic drag, no other forces like the Brownian force [21], Saffman's lift force [30] or the thermoforetic force [37] were included, since they mainly apply to sub-micron particles.

Additionally to the deterministic equations of motion, the dispersion of particles due to turbulence in the fluid phase is implemented. The two main methods accounting for the dispersion are the stochastic tracking (random walk) and the cloud model. The stochastic tracking introduces the effect of the instantaneous velocity field in the trajectory propagation of the individual particles. This way, the gas velocity v is fluctuating according to

$$v = \bar{v} + v' \tag{2.19}$$

instead of just using the middle speed $\bar{v}$. A discrete random walk model (DRW) determines the fluctuation v' and the trajectory is calculated repeatedly for a sufficient number of representative particles in order to allow for satisfactory statistics of the DRW [1].

For the cloud tracking method, the turbulent dispersion is seen as a statistical evolution of a particle cloud. The deviation of the particle concentration from the mean trajectory is given by a Gaussian PDF. Upon introduction of the particles into the domain, an expansion of the cloud takes place due to dispersion and the average number density at location x after the residence time t_{res} ($\langle n(x) \rangle$) is obtained by the total flow rate $\dot{m}$ and the PDF $P(x, t_{res})$ as:

$$\langle n(x) \rangle = \dot{m} P(x, t_{res}) \tag{2.20}$$

In the present work, only the stochastic tracking method was implemented.

2.2.4. Heat and mass Transfer

The interaction between the particles and the gas phase leads to a heat and mass exchange, which can be divided into three separate regimes in the case of an oxygen droplet:

1. Inert cooling/heating
2. Vaporization
3. Boiling

Each model represents a different temperature application region. The beginning of the vaporization is set when the droplet temperature exceeds the evaporation temperature T_{ev}. This quantity has no physical significance and is used only as a starting point for the evaporation model within the simulation (Note that throughout the present work, the terms "evaporation' and "vaporization" are used interchangeably and have the same meaning). When the droplet temperature reaches the boiling temperature T_b, the evaporation model ceases to apply and is replaced by the boiling law. For the temperature ranges smaller than both T_{ev} and T_b, the inert cooling/heating model is implemented to describe the heat and mass exchange.

It is possible to exclude one or more of these models from the simulation, simply by altering the values of T_{ev} and T_p. For example, by setting a very high value for T_b, which will not be surpassed in the simulation, one includes only evaporation within the model. Similarly, by setting the evaporation temperature lower than the initial particle temperature, the region of inert cooling/heating is omitted. The flow diagram in Fig. 2.5 describes the logical process behind the heat transfer models.

Inert cooling/heating

During the inert phase, there is no evaporation and hence no mass exchange with the gas phase. Only a temperature change is applied on the particle, according to Eq. 2.21:

$$m_p c_p \frac{\mathrm{d}T_p}{\mathrm{d}t} = hA_p(T_\infty - T_p) + A_p \epsilon_p \sigma_S \left(\frac{G}{4\sigma_S} - T_p^4 \right) \tag{2.21}$$

where c_p is the droplet heat capacity, h the convective heat transfer coefficient,A_p the surface are of the droplet, T_∞ the temperature of the continuous phase, ϵ_p

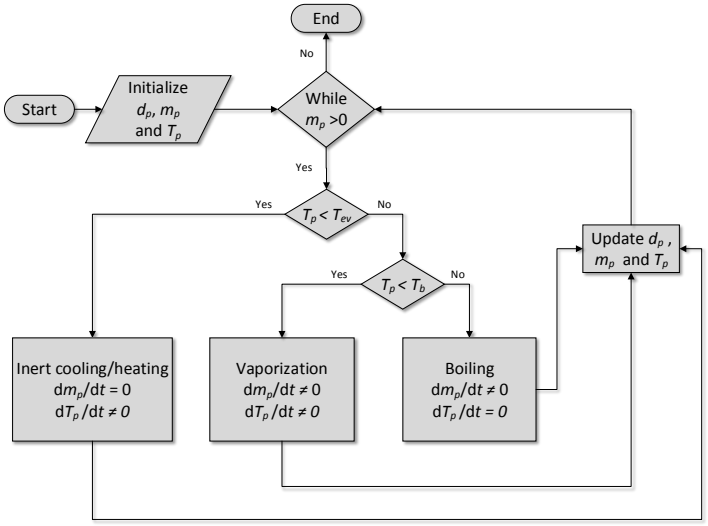

Figure 2.5.: Flow chart of heat transfer models

the particle emissivity, σ_S the Stefan-Boltzmann constant and G the incident radiation.

This model is applied until the droplet temperature reaches the vaporization temperature.

Vaporization

When the droplet comes in contact with the hotter surrounding gas, molecules on its surface with sufficient energy can escape and enter the gas phase. When this occurs, energy is being removed from the surface of the droplet (in the form of the enthalpy of vaporization for the molecules having escaped) and a cooling of the droplet occurs. The heat transfer leads to the prediction of the droplet temperature T_p according to Eq. 2.22:

$$m_p c_p \frac{\mathrm{d}T_p}{\mathrm{d}t} = hA_p(T_\infty - T_p) - \dot{m}_p \Delta h_{ev} + A_p \epsilon_p \sigma_S \left(\frac{G}{4\sigma_S} - T_p^4 \right) \tag{2.22}$$

where $\dot{m}_p$ the rate of evaporation and Δh_{ev} the enthalpy of evaporation.

The evaporation characteristics are mainly defined by the modeling of the convection coefficient and evaporation rate. For this purpose, two separate models are proposed by Fluent:

1. Diffusion Controlled Model
2. Convection/Diffusion Controlled Model

According to the Diffusion Controlled Model, the evaporation rate for an oxygen droplet is described by Eq. 2.23

$$\dot{m}_p = (2 + 0.6 Re_p^{1/2} Sc^{1/3}) \frac{D}{d_p} A_p M_{O_2} \left([O_2]_s - [O_2]_\infty \right) \tag{2.23}$$

with the diffusion coefficient D, the Schmidt number Sc being defined as $\mu/(\rho D)$, M_{O_2} being the molecular weight of oxygen and $[O_2]_s$ and $[O_2]_\infty$ the concentration of the vapor at the droplet surface and gaseous phase respectively. The assumption that the partial pressure of vapor on the droplet surface is equal to the saturation pressure $p_{sat}(T_p)$ is made and hence the difference of the two concentrations can be expressed by Eq. 2.24.

$$[O_2]_s - [O_2]_\infty = \frac{p_{sat}(T_p)}{RT_p} - X_{o2} \frac{p}{RT_\infty} \tag{2.24}$$

with X_{o2} representing the local bulk mole fraction of oxygen.

Within this model, the convective heat transfer is not modeled and hence the assumption $h = 0$ is implemented. Therefore according to Eq. 2.22 only the latent heat and the radiation (if present) contribute to the droplet temperature change. The effect of convection cannot be neglected in rocket combustion engines, due to the high gas speeds present and the high combustion temperatures leading to a significant heat rate being transferred to the droplets. For that reason, the diffusion based model was excluded from the simulations presented in the following chapters.

In the Convection/Diffusion Model on the other hand, the role of convection is included in the heat transfer equation. The mass loss is modeled according to

$$\dot{m}_p = (2 + 0.6Re_p^{1/2}Sc^{1/3})\frac{D}{d_p}A_p\rho\ln(1 + B_m) \tag{2.25}$$

with the Spalding mass number B_m given by

$$B_m = \frac{Y_{o2,s} - Y_{o2,\infty}}{1 - Y_{o2,s}} \tag{2.26}$$

which involves the vapor mass fraction on the surface of the droplet ($Y_{o2,s}$) and in the bulk gas ($Y_{o2,\infty}$). Furthermore, the heat convection is modeled based on

$$h = \frac{\ln(1 + B_m)}{B_m}(2 + 0.6Re_p^{1/2}Pr^{1/3})\frac{d_p}{\lambda_\infty} \tag{2.27}$$

where λ_∞ is the thermal conductivity of the bulk medium and Pr the Prandtl number.

The thermodynamic properties of oxygen including the saturation pressure and the latent heat were obtained from the National Institute of Standards and Technology (NIST) and can be found in the Appendix A. For the diffusion coefficient D, several approaches are available:

1. constant D
2. unity Lewis number
3. Chapman-Enskog model

The constant diffusivity is the simplest approach, and assumes the independence of the diffusion coefficient from the properties of the bulk medium. For the unity Lewis number approach, the diffusion coefficient is given by the gaseous phase properties as in Eq. 2.28:

$$D = \frac{\lambda}{\rho c_p} \tag{2.28}$$

Finally, for the Chapman-Enskog model, the pressure and temperature dependence of D is taken into account, yielding:

$$D = \frac{1.858 \cdot 10^{-3}T^{3/2}\sqrt{\frac{1}{M_1} + \frac{1}{M_2}}}{p\sigma_C^2\Omega} \tag{2.29}$$

where M_1 and M_2 represent the molar masses of the two gases involved in the diffusion process, and σ_C, Ω being the average collision diameter and the collision integral respectively. Details about the Chapman-Enskog model can be found in Appendix B. Due to the increased simplification of using a constant D and the lack of physical motivation behind the choice of a unity Lewis number, only the Chapman-Enskog model was included. Its deviation from the constant D model is also shown in Appendix B.

Boiling

As soon as the temperature of the droplet reaches the boiling temperature of oxygen, the boiling of the liquid droplet starts. This physical process takes place in the bulk of the particle as opposed to evaporation, which is a surface process. During the boiling of the droplet, the droplet temperature remains constant and equal to the boiling temperature T_b, which is a function of the surrounding pressure. The mass loss rate is then given by

$$\dot{m}_p = \frac{\pi d_p^2}{2} \frac{\mathrm{d}d_p}{\mathrm{d}t} \tag{2.30}$$

and

$$\frac{\mathrm{d}d_p}{\mathrm{d}t} = \frac{2}{\rho_p \Delta h_{ev}} \left[\frac{2\lambda_\infty (1 + 0.23\sqrt{Re_p})}{d_p} (T_\infty - T_p) + \epsilon \sigma_S \left(\frac{G}{4\sigma_S} - T_p^4 \right) \right] \tag{2.31}$$

In case no radiation is modeled, then the boiling law is modified to

$$\frac{\mathrm{d}d_p}{\mathrm{d}t} = \frac{4\lambda_\infty}{\rho_p c_{p,\infty} d_p} (1 + 0.23\sqrt{Re_p}) \ln \left(1 + \frac{c_{p,\infty}(T_\infty - T_p)}{\Delta h_{ev}} \right) \tag{2.32}$$

3. The Mascotte A-10 Test Case

One of the research programs with the purpose of assessing the complex phenomena involved in the operation of H_2/O_2 rocket engines has been developed by in a collaboration between ONERA, CNRS, Snecma and CNES. In order to improve the understanding and modeling of the physical and chemical processes taking place in LOX/GH_2 combustion, ONERA has developed the cryogenic test facility Mascotte. The properties of atomization, evaporation and combustion are experimentally examined in this combustor, with the purpose of using the obtained knowledge for the validation of CFD models [29].

3.1. Experimental Setup

A detailed description of the Mascotte test facility is given by Vingert and Habiballah in [35]. The chamber has a square cross section with a 50 mm edge length. The distance from the faceplate until the throat of the nozzle amounts to 478 mm, while the throat diameter is 15 mm. This leads to a contraction ratio between chamber and throat equal to $\epsilon_c = 14.1$ and to a characteristic chamber length

$$l^* = \frac{V_c}{A_t} = 6.6\,\mathrm{m} \tag{3.1}$$

which is defined as the quotient between chamber volume V_c and throat area A_t. By examining the values for the contraction ratio and the characteristic length, it is evident that the geometry of the chamber is not representative for common rocket engine applications, since most H_2/O_2 engines have $2.5 \leq \epsilon_c \leq 3.0$ and $0.7\,\mathrm{m} \leq l^* \leq 0.8\,\mathrm{m}$. Nevertheless the Mascotte facility and the A-10 case in particular have been extensively used for the investigation of the cryogenic combustion. A schematic overview of the Mascotte combustor geometry is given in Fig. 3.1.

The injection of the propellants takes place with a coaxial injector, whose geometry is described in Fig. 3.2 and Table 3.1.

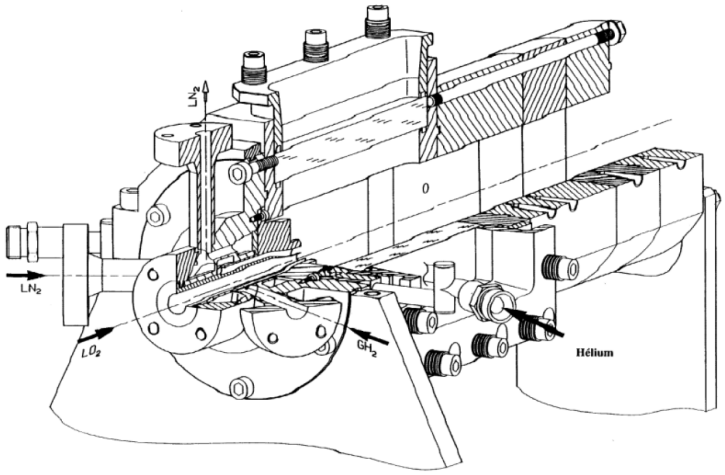

Figure 3.1.: The Mascotte combustor (Haidn)

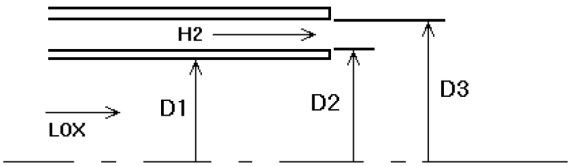

Figure 3.2.: The coaxial injector of the Mascotte A-10 case

Moreover, the chamber is equipped with an optical diagnostics system, which is made possible due to the quartz windows on the sides of the chamber. The windows allow for temperature and OH-emission measurements as described in Section 3.3 and are cooled by means of a helium film. The optical access is however restricted only to the first segment of the chamber and therefore does not provide a complete image of the combustion process.

Table 3.1.: Geometry of the Mascotte coaxial injector

Diameter	Value
D1	5.0 mm
D2	5.6 mm
D3	12.0 mm

3.2. Operating conditions of the A-10 case

The Mascotte combustor can operate in different pressure conditions and with different propellant combinations [35]. For the case of H_2/O_2 combustion, two subcritical (A and A-10) as well as one transcritical (A-60) tests (referring to the thermodynamic state of oxygen) have been performed and published. A summary of the operating conditions can be found in Table 3.2.

Table 3.2.: Operating conditions of the Mascotte H_2/O_2 tests

Test name	Pressure	$\dot{m}_{O_2}$	$\dot{m}_{H_2}$	OF	J
A	1 bar	50 g/s	15 g/s	3.3	13.4
A-10	10 bar	50 g/s	23.7 g/s	2.1	14.5
A-60	60 bar	100 g/s	70 g/s	1.4	13.8

The operating conditions can also be seen as points in the pressure-temperature diagram of Fig. 3.3. Note that for a better comparison, the reduced temperature T_r and p_r are used, with:

$$T_r = \frac{T}{T_c} \quad \text{and} \quad p_r = \frac{p}{p_c} \tag{3.2}$$

The critical pressures p_c and temperatures T_c for H_2 and O_2 are:

1. H_2 : p_c=12.96 bar, T_c=33.2 K
2. O_2 : p_c=50.46 bar, T_c=154.6 K

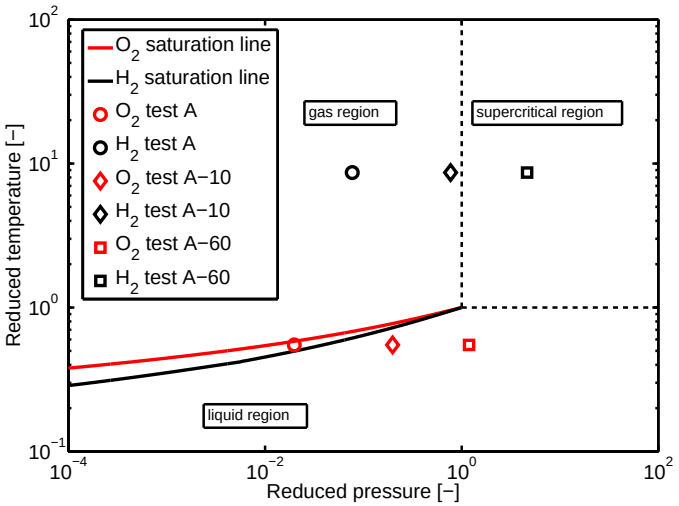

Figure 3.3.: Reduced temperature vs pressure diagram with saturation curve and the Mascotte operating points

One observes that both the oxidizer and the fuel are injected at subcritical conditions for the A-10 case. A summary of the initial conditions for the propellants is given in Table 3.3.

Table 3.3.: Propellant properties at injection for the A-10 case

Quantity	**H_2**	**O_2**
Temperature	287 K	85 K
Mass flow	23.7 g/s	50.0 g/s
Velocity	319 m/s	2.18 m/s
Density	0.84 kg/m^3	1170 kg/m^3

3.3. Experimental data

Due to the presence of the optical window, measurements of the temperature and the OH^* concentration are available for the A-10 case.

3.3.1. Temperature measurements

The measurement of the temperature field resulting from the turbulent combustion within the Mascotte chamber is measured based on the Coherent anti-Stokes Raman Spectroscopy (CARS) method. This relies on sending two laser beams with different frequencies through an optical medium (the hot gas in this case) and measuring the spectrum of the resulting beam, which gives information about the temperature and density fields. A detailed description of the method can be found in Begley et al. [5].

Due the below-stoichiometric mixture ratio of the A-10 case, the presence of oxygen is limited and therefore the H_2 and H_2O molecules were used as a Raman-active medium. The measurements used in the frame of this thesis are obtained from the published results of Candel [6] and Pourouchottamane [22], and have been obtained over a time period of 15 s at different locations along the chamber. The averaged values together with their respective uncertainties (standard deviation) are plotted in Fig. 3.4 along the axial position of the chamber. The axial position is measured from the faceplate, whereas the y values represent different distances from the axis of the chamber, with $y = 0\,\text{mm}$ being the axis and $y = 25\,\text{mm}$ the horizontal wall. The high values of the temperature's standard deviation can be interpreted as the outcome of a highly turbulent combustion.

By comparing the values in Fig. 3.4, it can be observed that the measured temperatures obtained by H_2 and H_2O emissions demonstrate significant discrepancy between each other, mainly within the reaction zone. This can be explained by the high turbulence degree of the flow, which leads to an interchange between reaction zones and non-reactive regions over time. Since the H_2O molecules mainly reside in the non-reactive regions (they are the reaction products), they also have a smaller temperature. When these molecules interact with the incoming LOX droplets, they transfer part of their energy to the colder liquid and hence demonstrate a smaller temperature in the CARS measurements. For axial positions further downstream, the agreement between H_2 and H_2O measurements increases, implying a better mixing of the two gases.

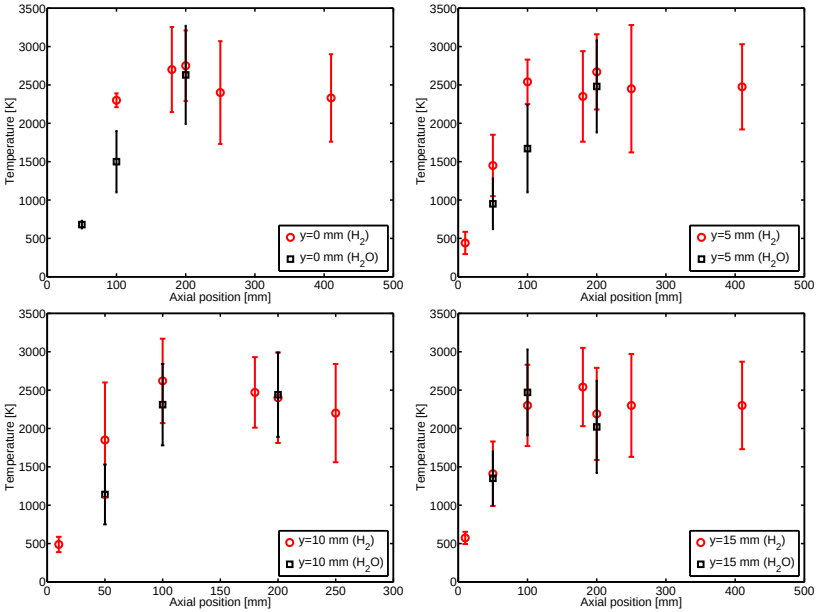

Figure 3.4.: CARS temperature measurements of H_2 and H_2O emissions at y=0 mm, y=5 mm (top) and y=10 mm, y=15 mm (bottom)

3.3.2. OH^* emissions

Useful information about the flame front can be given by observing the concentration of Hydroxyl-radicals (OH^*) within the flow field. At high temperatures, OH molecules are excited and upon de-excitation emit ultraviolet (UV) radiation. Therefore, by capturing the intensity of this UV rays, the reaction zone can be identified.

In the A-10 Mascotte case, the OH^* emissions were captured with a Charged Coupled Device (CCD), perpendicularly to the quartz windows. Of course, this implies that only the integrated radiation flux along the depth direction can be measured and not the local OH^* concentration. To obtain the local field, an Abel-transformation has to be applied, which takes the assumption of an

axissymmetric flame, thereby ignoring the effect of the corner in the quadratic chamber. The averaged measured OH^* field as well as the Abel-transformed one are shown in Fig. 3.5.

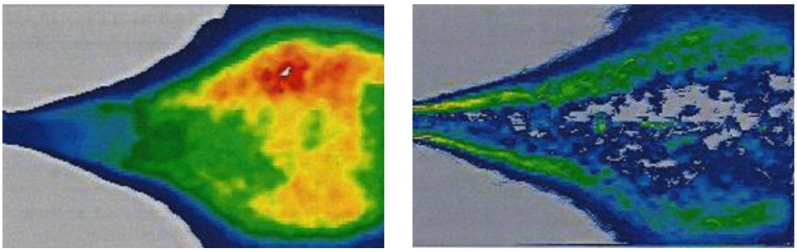

Figure 3.5.: Measured (left) and Abel-transformed (right) OH^* field

However, the instantaneous OH^* field does not fully represent the complete OH concentration, since there are OH molecules which do not get excited and hence not emit UV-light in the reaction zone. For that reason, comparing the experimental results of Fig. 3.5 with the numerically obtained OH concentrations is not completely justified. To overcome this, the *a posteriori* method proposed by Fiala et al. [13] was examined, according to which, the calculated OH field can be used to calculate the OH^* concentration in the chamber. According to this model, the OH^* and OH molecules are in thermal equilibrium (assuming only thermal reactions and quenching) and therefore the concentration of OH^* ($[OH^*]$) is given by

$$[OH^*] = [OH] \cdot \exp\left(\frac{-\Delta g^0}{RT}\right) \tag{3.3}$$

where the temperature T and the OH-concentration $[OH]$ are already known as results of the simulation. The molar Gibbs enthalpy of formation Δg^0 can be approximated by the energy emitted during the spontaneous de-excitation of the molecule as in

$$\Delta g^0 = \frac{h_P c}{\lambda_{OH}} N_A \tag{3.4}$$

with h_P being the Planck constant, c the speed of light, N_A the Avogradro number and $\lambda_{OH} = 308\,\text{nm}$ the wavelength of the emitted light. The effect of

this method on the final result was examined in Section 4.2.1.

4. 2D Simulations

The simulation of the Mascotte A-10 case was carried out with the commercial code Fluent. For this purpose, an axisymmetric simulation was set up, assuming that the circumferential gradients in the flow vanish. Different models and initial conditions were examined for these two-dimensional calculations as described in Section 4.3.

4.1. Geometry and Mesh

Since the simulation takes place in a 2D computational domain, the geometry of the Mascotte combustor had to be slightly modified. In order to account for the fact that the square cross section would be modeled by a cylinder, the radius of the chamber was changed to $r_{chamber} = 28.2\,\text{mm}$, which is slightly larger than the distance between axis and wall in the 3D case, i.e. 25.0 mm. This radius ensures that the volume of the chamber remains the same in the 2D and 3D cases. Not modifying the radius would result in a slightly larger chamber pressure (due to the smaller volume) and hence to a different density of H_2, thereby altering the momentum flux ratio.

A further modification included the injection of the liquid oxygen phase, for which the suggestion of Vingert and Habiballah was implemented [35]. According to that, the liquid core of the oxygen flow is modeled as a cone. The height of the cone is given by the radius of the oxygen inlet and its length L_c is empirically determined and equal to 7.8 mm. This cone, which can be seen in Fig. 4.1, serves as the injection surface for the particles of the discrete phase.

For the discretization of the computational domain, a mesh study was carried out. The initial dimensions of the cells in the mesh were chosen at 0.5 mm in radial direction and 1.0 mm in axial direction. A simulation without the discrete phase was carried out with the mesh and the number of cells was gradually increased, until no dependence of the final solution on the mesh was observed any more. This occurred at the second iteration, leading to a mesh resolution of 0.25 mm in radial and 0.5 mm in axial direction and 126100 total elements.

The resolution near the walls was established so as to obtain y^+ close to 1. However, the boundary layer flow is not so critical, since no experimental values for the heat flux are available.

The influence of the mesh resolution on the calculations with discrete phase was found to be not so critical. The trajectories of the particles are calculated independently from the existing mesh and a rule of thumb is that a droplet should stay for 3-5 time steps within one cell before moving to the next one. Practically this is modified by changing the time step of the Lagrange tracking and not by altering the mesh itself. Finally, a mesh with too fine resolution could create divergence problems in the case of Lagrange tracking. This could occur when a high mass, energy or impulse source from the discrete phase, was to be implemented to the nodes of a cell, leading to high gradients. This is avoided in general by averaging the source terms over the neighboring cells, leading to a smoothening of the gradients [1].

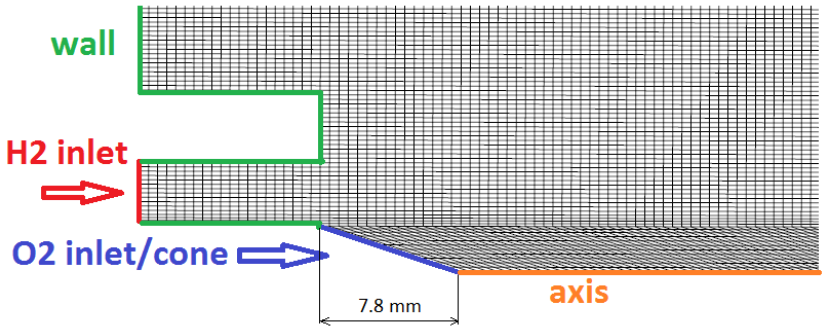

Figure 4.1.: Close-up view of the injector and the liquid core in the computational domain

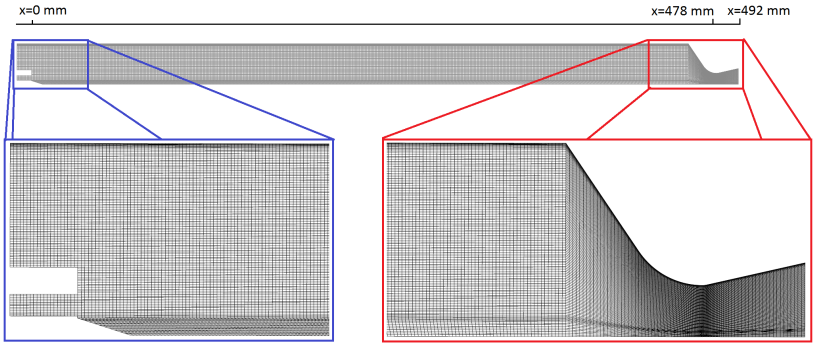

Figure 4.2.: 2D mesh of the Mascotte combustor

4.2. Boundary Conditions

This section describes the main considerations behind the choice of the boundary conditions for the 2D simulation.

GH_2 inlet

A mass flow boundary condition was defined for the hydrogen flow, with $\dot{m}_{H_2} = 0.05\,\mathrm{kg/s}$ and a total temperature $T_{H_2,t} = 290.5\,\mathrm{K}$, which resulted from the measured static temperature (287 K), measured density ($0.84\,\mathrm{kg/m^3}$) and velocity (319 m/s).

LOX inlet

For the LOX inlet, a solid cone was used, as described in Section 4.1. Along this cone, 15 injection positions were chosen from which the liquid particles could enter the domain. The velocity of the droplets was set to 10 m/s, which is the experimentally measured value 30 mm downstream of the injector and is proposed by Vingert et al. [35]. The initial temperature of the droplets was defined to be 85 K and the corresponding density $1170\,\mathrm{kg/m^3}$.

For the diameter of the particles, a Rosin-Rammler distribution was used with

the following parameters in Table 4.1. These values were fitted to the experimental data and are stated in [35].

Table 4.1.: Rosin-Rammler distribution parameters for the LOX particles

Quantity	**Value**
$\boldsymbol{n}$	2.25
$\boldsymbol{d_{ref}}$	130 μm
$\boldsymbol{d_{min}}$	1 μm
$\boldsymbol{d_{max}}$	300 μm

d_{min} and d_{max} are the limiting diameters of the distribution. Fluent provides a built-in tool for the Rosin-Rammler distribution, which requires the data in Table 4.1 as input as well as the number of total diameters simulated, N. For each injection point, N parcels are injected, each one with a different diameter, which is dictated by the Rosin-Rammler parameters. In the present simulations the number of diameters was set to 40.

The resulting diameter distribution stemming from Fluent was validated with the expected theoretical one. For a total mass flow of 0.05 kg/s, 6 injection points were defined for this validation and a calculation of 100 time steps for the liquid phase was carried out. The information about the computational parcels was post-processed and this way the number of physical particles/droplets was plotted as a function of size in Fig. 4.3.

A satisfying agreement is observed between the theory and the measured distribution. The only regions were the Fluent distribution over-predicts the number of particles is for $d \leq d_{min}$ and $d \geq d_{max}$. The histogram summarizes all particles with $d \leq d_{min} = 1\,\mu$m in the first bar, thereby appearing bigger than the theoretical value, which only assumes $d \geq d_{min} = 1\,\mu$m. A similar effect is observed for diameters close to $d_{max} = 300\,\mu$m.

Apart from the diameter distribution, the injection direction of the LOX droplets also influences the solution. Vingert et al [35] propose an injection angle of the particles varying with their position on the solid core. This empirical correla-

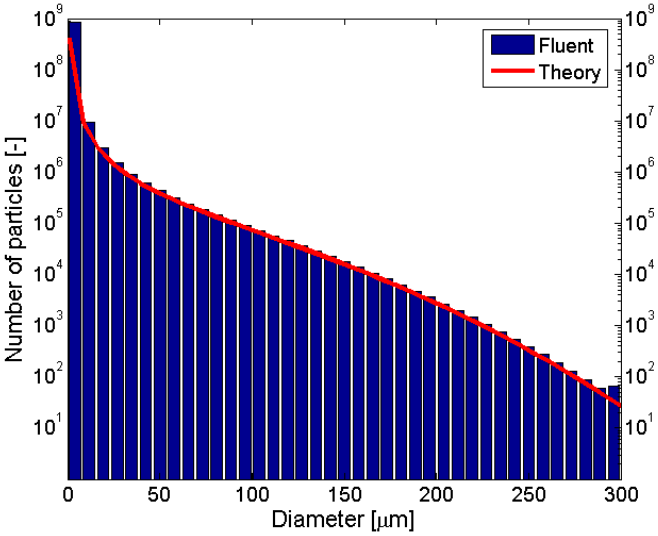

Figure 4.3.: Number of droplets in the Fluent simulation and the expected profile according to the Rosin-Rammler distribution

tion for the injection angle θ is given by Eq. 4.1.

$$\theta = \arctan\left[\frac{\frac{D_1}{2}\left(1-\frac{x}{L_c}\right)}{x+\frac{D_1}{2\tan\theta_0}}\right] \tag{4.1}$$

The angle θ_0 corresponds to $x = 0$ and is given empirically by

$$\tan\theta_0 = 0.68\left(\frac{v_{H_2}}{v_{O_2}}-1\right)\sqrt{\frac{\rho_{H_2}}{\rho_{O_2}}} \tag{4.2}$$

where $v_{H_2} = 319\,\mathrm{m/s}$, $v_{O_2} = 2.18\,\mathrm{m/s}$, $\rho_{H_2} = 0.84\,\mathrm{kg/m^3}$ and $\rho_{O_2} = 1170\,\mathrm{kg/m^3}$. This leads to a maximal angle for $x = 0$ equal to approximately $\theta_0 = 70°$. This proposed injection angle distribution was compared with other values for θ_0 as shown in Section 4.3.1. To illustrate the variation of the injection angle, the

injected particles from Fluent are shown in Fig. 4.4. The first 100 time steps were calculated and the positions of the particles can be used to visualize their injection velocity. This intialization of the particles' velocity can be directly compared to Fig. 4.5, where a uniform injection angle of 0° was used. The particles are colored based on their diameter, in order to demonstrate that in each injection, the droplet sizes follow the Rosin-Rammler distribution.

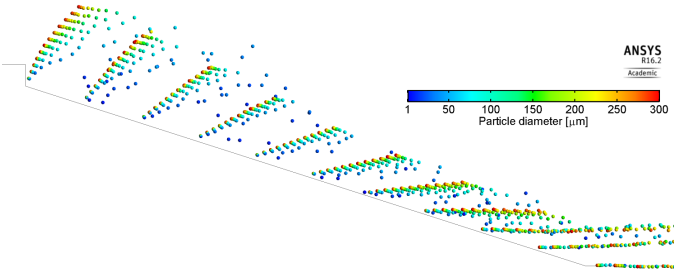

Figure 4.4.: Trajectories of injected particles for the distribution in Eq. 4.1, colored by particle size

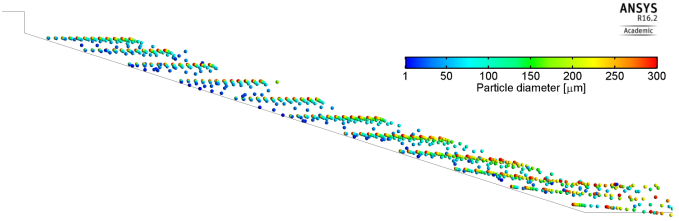

Figure 4.5.: Trajectories of injected particles for uniform 0° injection angle, colored by particle size

Nozzle

The nozzle exit was defined as a pressure outlet with a static pressure of 1 bar behind it. The discrete phase particles reaching the nozzle outlet, escape the computational domain.

Walls

The thermal boundary condition for all walls was defined as adiabatic, since no information about the temperature of the wall or the measured heat flux was provided in the experimental data. Although the A-10 chamber window is cooled by a Helium film, this was not included in the simulation model. The main reason is that including this extra inert gas component would not be compatible with the use of the mixture fraction description and would require a detailed reaction mechanism. Moreover, it would induce further degrees of freedom in the model, without providing any additional experimental data to compare with, since no measurements of the Helium temperature or concentration is available.

The boundary condition for the discrete phase at the walls was defined to be reflective, meaning that the particle impulse tangent to the walls remains unchanged and the component normal to the wall is conserved in magnitude but changes direction. Fluent provides also the possibility of modeling the formation of a liquid film on the walls of the chamber, which can evaporate or even break-up into further particles. This option is however only available for transient simulations. A further modeling option is assuming that the droplets evaporate completely upon collision to the chamber walls. Upon collision, the entire mass instantaneously passes into the vapor phase and the fate of the particle is terminated. This would sufficiently describe a form of "flashing" of the liquid droplets upon collision with a hot chamber wall. The effect of this flashing was examined in Section 4.3.4.

4.2.1. Initial solution

In order to facilitate the convergence of the simulation with the discrete phase, a solution of the combustion problem was calculated by replacing the liquid oxygen with gaseous oxygen with the same mass flow rate. Of course, the physics of the problem change significantly, since the lower density of the GO_2 and its higher velocity, lead to a different momentum flux ratio. Nevertheless, using the obtained fields as an initial solution for the following simulations

reduced computational time. In the case simulated, the injection velocity of the oxygen had a 0° angle with the chamber axis. The temperature field and OH-mass fraction are plotted in Fig. 4.6 and Fig. 4.7. The maximal gas temperature is approximately 2900 K.

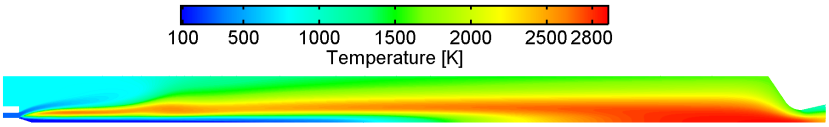

Figure 4.6.: Temperature field for the GH_2/GO_2 solution

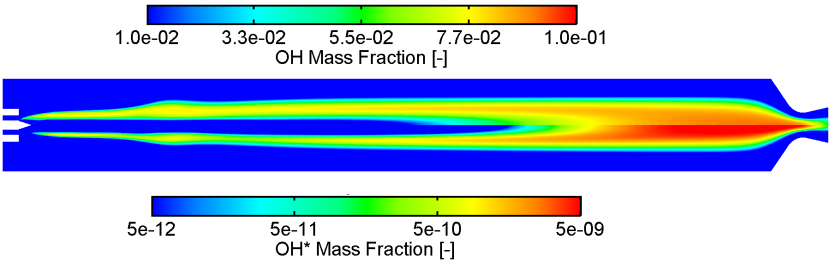

Figure 4.7.: OH^* and OH field for the GH_2/GO_2 solution

It is evident from Fig. 4.7, that the mass fraction of the hydroxyl-radicals (OH^*) is approximately eight (8) orders of magnitude smaller than the OH mass concentration. Qualitatively, one also observes that the OH^* field demonstrates a thinner accumulation region compared to the OH field. This occurs due to the excess kinetic energy which is required to excite the OH molecules, which takes place only at regions with high temperatures, according to Eq. 3.3. Therefore, the excited molecules are only limited in the region of the flame front with the highest temperature. Since the qualitative difference between the OH and OH^* fields is not negligible, the comparisons between the numerical results and

the experimental emissions presented in Fig. 3.5 will take place based on the a posteriori method presented in Section 3.3.2.

4.3. Simulation Results

4.3.1. Effect of the droplet injection angle

A distribution for the injection angle of the liquid oxygen droplets has been proposed in Eq. 4.1, which demonstrates an increase in the injection angle from 0° on the axis ($y = 0\,\text{mm}$) up to 70° at $y = D_1/2 = 2.5\,\text{mm}$. However, previous works [10] have shown upon examination of further angle distributions, that the numerical results obtained with a constant 0° injection angle, agree with the experimental measurements the most. For that reason, the effect of the injection angle was examined and the results are presented in this section.

In order to ensure, that a comparison between the different angle distributions is possible, all other boundary conditions and models were used consistently as described in Table 4.2. According to Eq. 4.1, the injection angle varies from 0° to θ_0. The maximal injection angle θ_0 was experimentally approximated as $\theta_0 \approx 70^\circ$. Two further cases where simulated: One for a maximal injection angle $\theta_0 = 0^\circ$ and one for $\theta_0 = 30^\circ$. The results of the temperature field for the three cases can be seen in Fig. 4.8. The dark line represents the stoichiometric line and is used to approximate the flame front, since the points of stoichiometric composition correspond to the points with optimal mixing.

A strong dependence of the flame length on the injection angle is observed. The 0° case demonstrates a typical bulge in the flame, whereas the two cases with non-zero injection angles show a more or less straight flame. Moreover, the length of the flame can be compared by examining the intersection point of the stoichiometric line with the chamber axis. The flame length seems to dramatically decrease with increasing injection angle. This result coincides with the investigation on the injection angle, which was presented by Dyke in [10].

The behavior of the OH^* radicals is also similar, as shown in Fig. 4.9. In the 70° and 30° cases, the radicals are accumulated in a very thin region, which does not extend in radial direction and therefore does not resemble the experimental measurements. On the other hand, the 0° injection produces an OH^* field quite similar to the experimental Abel-transformed image. Although the radicals' region in the simulation is thinner, the axial position, at which

Table 4.2.: Simulation settings for the examination of the injection angle

Setting	Value
Heat/Mass Transfer model	Vaporization
Vaporization Model	Diffusion/Convection based
Diffusion constant	Chapman-Enskog model
Turbulence Model	$k-\epsilon$
Wall Treatment	Enhanced Wall Treatment
Turbulent Schmidt number Sc_t	0.85
Turbulent Prandtl number Pr_t	0.85
Combustion Model	Equilibrium chemistry
Wall Heat Boundary Condition	Adiabatic
Wall Boundary Condition for DP	Reflection
Discrete Phase Turbulence	Random Walk
Rosin-Rammler parameters	$n = 2.25$, $d_{ref} = 130\,\mu$m
Rosin-Rammler number of diameters	$N = 40$
H_2 mass flow	23.7 g/s
H_2 inlet total temperature	290.5 K
O_2 mass flow	50 g/s
O_2 inlet temperature	85 K
O_2 inlet speed	10 m/s

the flame bulge is present, as well as the radial extension, show a satisfactory agreement.

The injection angle directly affects the particle trajectories, which in turn influences the locations at which they evaporate. In order to investigate this effect in detail, the mass source of the discrete phase was plotted in Fig. 4.10. One can observe, that even for the 0° case, there are particles moving at an angle with respect to the chamber axis. These particles are deviated from the initial path, which was parallel to the axis, due to interaction with the hydrogen inlet. The H_2 inlet has a high velocity (319 m/s) compared to the droplets' speeds (10 m/s). As Fig. 4.8 shows for 0°, the injected hydrogen also departs from its

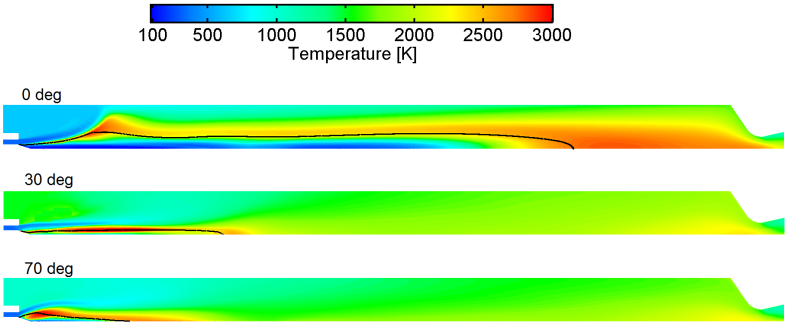

Figure 4.8.: Temperature field in the thrust chamber for different injection angles

initial parallel-to-axis flow due to the flame's bugle. Therefore, it has a radial impulse component, which can be transferred to the oxygen particles in the form of drag forces. This explains why there are non-zero mass sources close to the chamber walls for the 0° case in Fig. 4.10. These particle which are deviated significantly by the drag acceleration, must have a small mass (and hence small diameter) and this can be also justified by optically following their trajectories in Fig. 4.10. After being reflected to the wall, their mass source (evaporation rate) decays very fast, which implies that they have completely evaporated before reaching the chamber axis again. The heavier particles on the other hand are almost unaffected by the hydrogen inflow and continue their trajectories parallel to the chamber axis and evaporate when passing through the hot flame front.

The 30° and 70° cases also have particles with radial impulse components, as one can deduce from the mass source plot. These particles however, are not only light droplets which have been deviated by the injected hydrogen, but also larger droplets, following the injection pattern as shown qualitatively in Fig. 4.4. These particles, having a bigger mass, continue their trajectory and undergo even multiple reflections on the wall before evaporating completely or escaping through the nozzle. An indicator for this phenomenon is the presence of large mass sources for radial positions close to the wall at axial locations

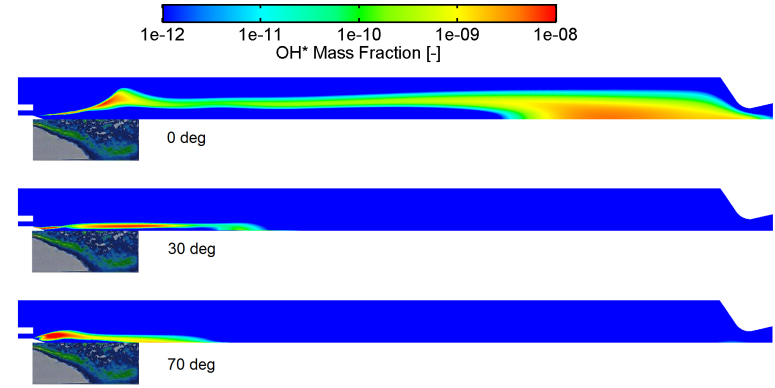

Figure 4.9.: OH^* field in the thrust chamber for different injection angles and comparison to experimental data

downstream of the flame front, which only occurs for 30° and 70° in Fig. 4.10.

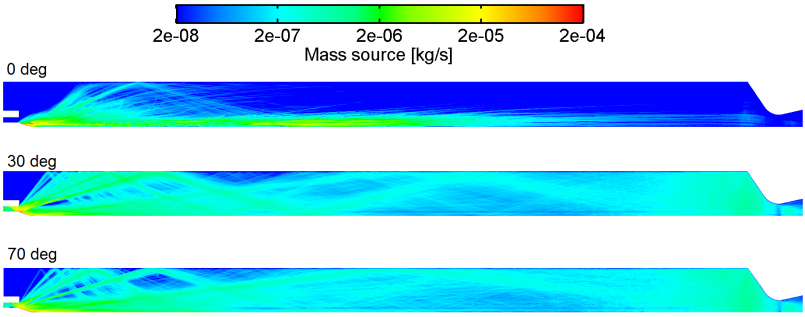

Figure 4.10.: Mass source field in the thrust chamber for different injection angles.

Fig. 4.11 serves as a further justification of this theory. Here the mass sources are summed along the radial direction and their sums are plotted as a function of the axial location. It is evident, that for the 0° injection angle, the majority of the particles evaporates before reaching the nozzle. For the larger injection angles on the other hand, due to the reflections on the wall, particles escape the combustion zone without evaporating completely, leading to a higher mass source in the nozzle.

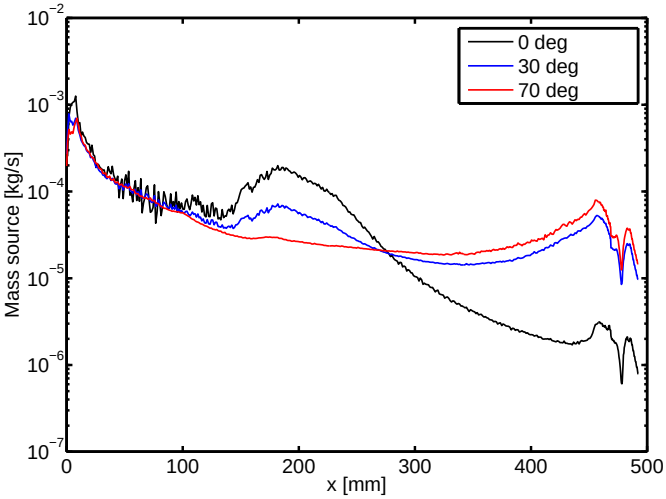

Figure 4.11.: Summed mass source due to evaporation along the chamber axis for different angle distributions

Finally, the mass sources were allocated to three zones in the thrust chamber:

1. Recirculation zone
2. Combustion chamber
3. Nozzle

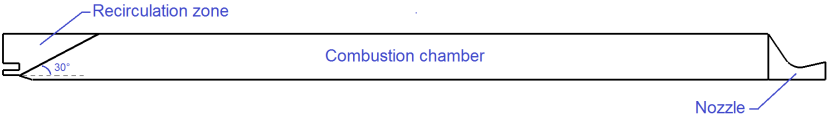

Figure 4.12.: Definition of the three zones for the mass source calculation in the computational domain

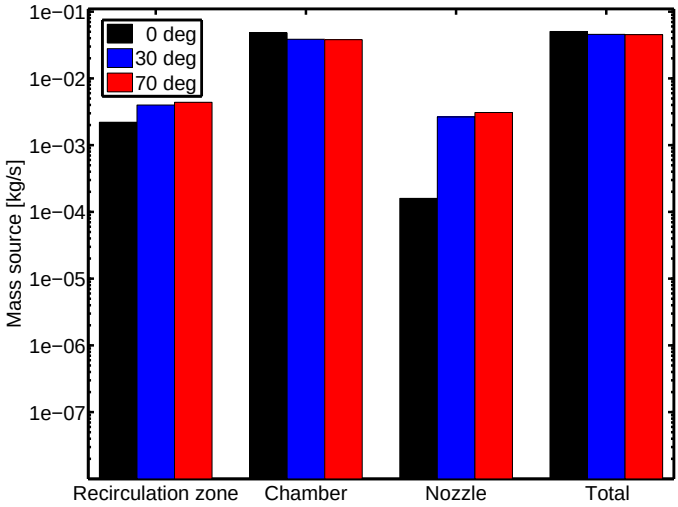

Figure 4.13.: Mass source due to evaporation in the three zones for different angle distributions

The geometrical characteristics of each zone are shown in Fig. 4.12. Fig. 4.13 can be used to compare between the different injection angles. As expected, a higher injection angle leads to more particles entering the recirculation zone and hence evaporating there partially or even completely. Moreover, the 0° case leads to much lower mass source in the nozzle (1 order of magnitude lower than for the higher angles) and to a higher mass source in the combustion

chamber and in total.

All in all, the 0° injection angle was found to provide more realistic results for the flame front and also showed a better agreement with the experimental data. Therefore, it is the one that will be used as a boundary condition for the oxygen droplets for the further simulations in this thesis.

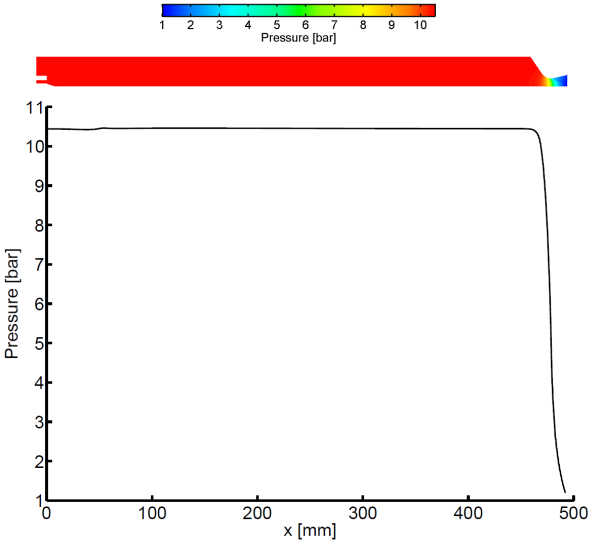

Figure 4.14.: Pressure field in the combustion chamber and nozzle and axial plot of the average pressure

In the simulations presented in this section, the properties of liquid oxygen (density, specific heat capacity, enthalpy of vaporization) were treated as pressure dependent. However, modeling them as pressure-independent would accelerate the DP calculations. In order to examine whether this simplification is righteous or not, the pressure field in the thrust chamber is illustrated in Fig. 4.14. The static pressure remains constant at approximately 10.4 bar throughout the length of the chamber and only drops in the nozzle. Since

approximately 96 % of the droplet mass evaporates in the chamber, where the pressure is constant (see Fig. 4.13), the effect of the nozzle is negligible and the pressure-independent properties for the liquid oxygen can be utilized without jeopardizing the accuracy of the simulation.

4.3.2. Examination of flame length

The investigation of the injection angle in Section 4.3.1 demonstrated that a uniform injection angle of 0° matches the experimental data of temperature in the best manner. However, the OH^* measurements are restricted in the first 70 mm after the injector and therefore cannot provide information about the total length of the flame, so no comparison is possible.

In Fig. 4.8, the length of the flame appears to be close to 355 mm from the injector and Fig. 4.9 indicates that a significant OH^* radicals production takes place even in the converging part of the Laval nozzle. These two characteristics do not coincide with common experience in the field of single-element combustion chambers. Usually, the flame front stops before reaching the nozzle of the engine, in order to ensure complete combustion of the reacting propellants. Specifically, in the Mascotte chamber with $l^* = 6.6\,\mathrm{m}$, which is much longer than the typical H_2/O_2 characteristic length, the end of combustion is expected to be much closer to the injector than in the case of the obtained simulation results.

For that reason, two sets of simulation parameters were altered with the aim to examine their effect on the flame length:

1. Oxygen inlet speed
2. Turbulent dimensionless numbers (Sc_t and Pr_t)

Firstly, a reduced oxygen inlet speed implies a smaller "resistance" of the droplets to the flow and hence the discrete phase can follow the gas phase easier. This reduces the number of droplets with high radial momentum and also the reflections on the wall and leads to particles evaporating in axial positions closer to the injector and hence to gaseous oxygen being present in shorter axial positions. Therefore, the combustion is completed further upstream compared to a case with higher initial droplet speed and results in a shorter flame front.

According to the A-10 case description, the initial flow velocity of the oxygen stream is 2.18 m/s. Measurements 30 mm downstream of the injector provided a value of 10 m/s for the droplet speed and therefore this is the value commonly used as a boundary condition for the oxygen inlet [10] and was also implemented in the calculations of the present thesis so far. Therefore, in order to examine the effect of a shorter speed, the value of 2.18 m/s seems like a reasonable choice.

The second set of parameters, the turbulent Schmidt and Prandtl numbers have a direct influence on the turbulent transport quantities of the mixture. For the simulations in the previous sections, the values $Pr_t = 0.85$ and $Sc_t = 0.85$ were implemented. Experience in the field of CFD simulations in single-element and small-scale rocket engines at the Department of Flight Propulsion at the TUM, have shown that choosing the parameters as $Pr_t = 0.90$ and $Sc_t = 0.60$ delivers good agreement with experimental data. The lower turbulent Schmidt number can be translated to a higher turbulent diffusivity D_t ($Sc_t = \mu_t/(\rho D_t)$) and hence to a better mixing of the gaseous hydrogen and oxygen. A better mixing implies also that the combustion process requires shorter distance to be completed and hence the flame length is expected to be reduced compared to a case with higher Sc_t. For that reason, this variation was also examined.

The resulting four combinations are summarized here:

1. v=10 m/s, $Pr_t = 0.85$ and $Sc_t = 0.85$
2. v=10 m/s, $Pr_t = 0.90$ and $Sc_t = 0.60$
3. v=2.18 m/s, $Pr_t = 0.85$ and $Sc_t = 0.85$
4. v=2.18 m/s, $Pr_t = 0.90$ and $Sc_t = 0.60$

The first case has already been simulated and presented in Section 4.3.1. The temperature field for the remaining three combinations was compared to the reference case (v=10 m/s, $Pr_t = 0.85$ and $Sc_t = 0.85$) as can be seen in Fig. 4.15. The expected outcome was observed, with both effects (lower injection speed and higher Sc_t) leading to a shorter flame. The combination of these two changes (third plot in Fig. 4.15) demonstrates the shortest flame front and also a thicker flame. A summary of the maximal combustion temperature and of the flame front's distance from the injector is given in Table 4.3.

In order to establish which one of the four cases fits the experimental data with the best agreement, the temperature profiles along the axial direction

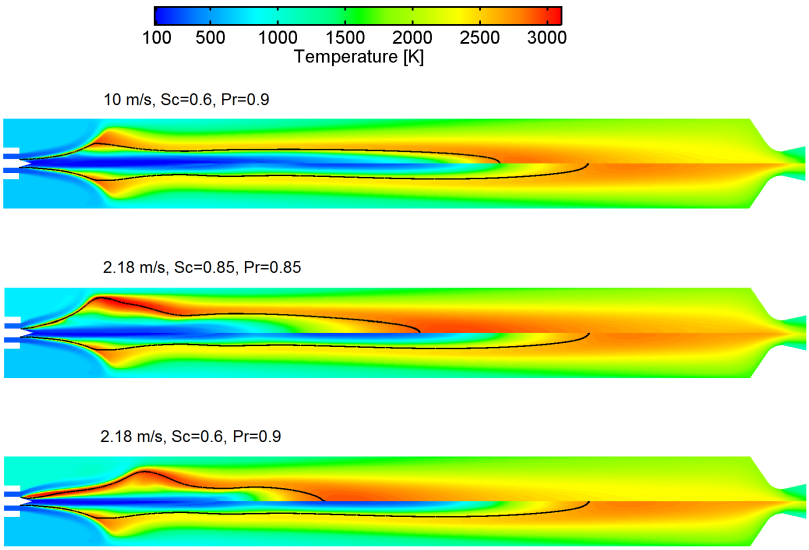

Figure 4.15.: Temperature field for various combinations of droplet injection speed and Sc_t/Pr_t

were examined for different radial positions, as presented in Fig. 4.16. For the higher radial positions (y=10 mm and y=15 mm) all combinations seem to match the measurements within the uncertainty limits. Closer to the chamber axis however (y=0 mm and y=5 mm), the case with v=2.18 m/s, $Pr_t = 0.90$ and $Sc_t = 0.60$ demonstrates the best fit. It still fails to capture the correct location of the flame on the axis (y=0 mm) but provides a better agreement than the other cases.

For that reason, a modification of the implemented boundary conditions and turbulence model settings was carried out. After the modifications of Section 4.3.1 and 4.3.2, the updated settings for the simulation are summarized in Table 4.4. The values highlighted in bold represent the modified settings.

Table 4.3.: Maximal combustion temperature and flame length for the different combinations of droplet inlet speed and Sc_t/Pr_t

Case	Max. temperature	Distance of flame front from injector
1	2900.2 K	357 mm
2	2945.5 K	302 mm
3	3015.2 K	251 mm
4	2967.7 K	191 mm

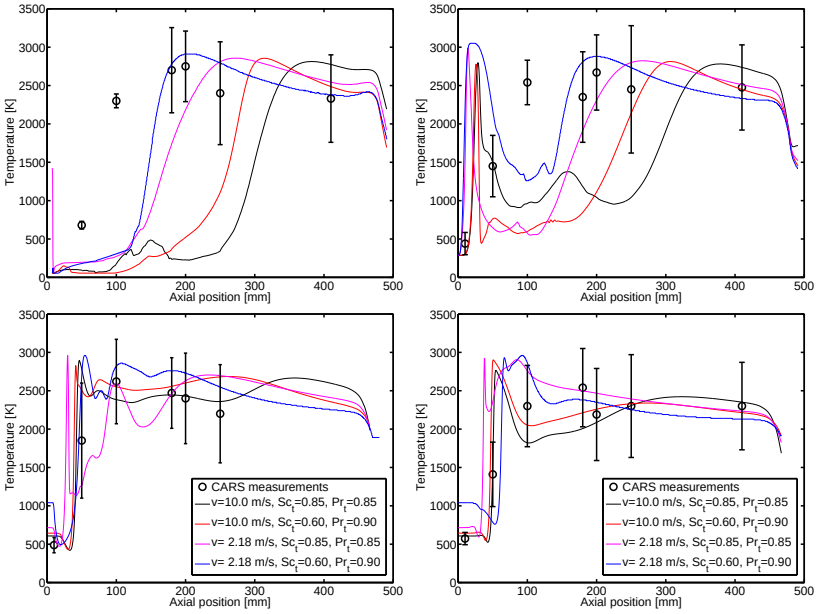

Figure 4.16.: Comparison of CARS temperature measurements with CFD results at y=0 mm, y=5 mm (top) and y=10 mm, y=15 mm (bottom) for various combinations of DP injection speed and Sc_t/Pr_t

Table 4.4.: Updated simulation settings

Setting	Value
Heat/Mass Transfer model	Vaporization
Vaporization Model	Diffusion/Convection based
Diffusion constant	Chapman-Enskog model
Turbulence Model	$k-\epsilon$
Wall Treatment	Enhanced Wall Treatment
Turbulent Schmidt number Sc_t	**0.60**
Turbulent Prandtl number Pr_t	**0.90**
Combustion Model	Equilibrium chemistry
Wall Heat Boundary Condition	Adiabatic
Wall Boundary Condition for DP	Reflection
Discrete Phase Turbulence	Random Walk
Rosin-Rammler parameters	$n = 2.25$, $d_{ref} = 130\,\mu$m
Rosin-Rammler number of diameters	$N = 40$
H_2 mass flow	23.7 g/s
H_2 inlet total temperature	290.5 K
O_2 mass flow	50 g/s
O_2 inlet temperature	85 K
O_2 inlet speed	**2.18 m/s**
O_2 injection angle	**0** $^\circ$

4.3.3. Comparison of evaporation models

The calculations performed in Sections 4.3.1 and 4.3.2 utilized the Vaporization model based on Diffusion/Convection Evaporation as explained in Section 2.2.4. The choice of the heat and mass transfer model directly influences the interaction between the discrete particles and the gas phase and for that reason the investigation of different models was considered to be of interest for the simulation of the A-10 case. For that purpose, four different models were implemented and compared to each other. All four cases included a combination of the models described in 2.2.4: inert cooling/heating, vaporization and boiling. The combination was carried out by modifying the evaporation temperature T_{ev} and the boiling temperature T_b. The settings of the four simulations are summarized in Table 4.5. All the remaining boundary conditions and modeling settings are the same as in Table 4.4.

Table 4.5.: Settings for the comparison of the heat and mass transfer models

Model description	T_{ev}	T_b	**Radiation**
Evaporation	55.00 K	5000.00 K	No
Boiling	119.49 K	119.50 K	No
Evaporation & Boiling	55.00 K	119.50 K	No
Evaporation, Boiling & Radiation	55.00 K	119.50 K	Yes

The first model (**Evaporation**) is the one implemented so far in the calculations and will serve as a reference. According to it, the evaporation temperature (55 K) is lower than the injection temperature of the liquid oxygen droplets (85 K) and therefore no inert heating/cooling takes place, since the evaporation begins right after the injection. The boiling temperature (5000 K) is chosen much higher than the expected combustion temperature, in order to ensure that no boiling takes place. This way the droplets undergo only the process of surface evaporation until their mass completely turns into gas or they escape through the nozzle. In the case of the **Boiling** model, the injected particles are not subject to evaporation. Their mass transfer only takes place as soon as they reach the boiling temperature of 119.5 K. This corresponds to the dew point of oxygen at 10 bar. Upon injection, the droplets exchange heat

with the gas phase through inert heating/cooling until they reach the evaporation temperature. This has been deliberately set right below the boiling temperature, to ensure that virtually no evaporation takes place. The evaporation model in Fluent cannot be completely switched off and every droplet must undergo evaporation before beginning to boil. Therefore, by picking T_{ev} suitably, the stage of evaporation can be by-passed. The droplets start boiling and keep their temperature constant at T_b, until they disappear or escape the domain.

In the third case examined here, a combined **Evaporation and Boiling** model is implemented. According to this, the injected particles undergo vaporization until reaching $T_b = 119.5\,\mathrm{K}$, when boiling starts. This model is thought to represent the reality more effectively, since it incorporates not only surface phenomena (evaporation) but also bulk ones (boiling), which become important when the dew point of a substance is reached. Finally, the fourth model (**Evaporation, Boiling and Radiation**) is identical to the third one, with the exception that radiation phenomena are included. The P-1 model [1] was used and the emissivity and scattering factor for liquid oxygen droplets were both set to 0.3.

The temperature field of the gas phase in the thrust chamber for the four implemented models is shown in Fig. 4.17. One can observe that the Evaporation model produces the longest flame, whereas the Boiling model produces the shortest one. This is expected when thinking about the heat transfer laws included. The droplets used in the Boiling model only undergo an inert heating period before they begin to boil, which quickly increases their temperature. This way T_b is reached in short distance from the injector and the mass transfer is initiated. Droplets undergoing evaporation on the other hand, do not raise their temperature as fast, since the vaporization of oxygen on their surface actually serves as a cooling, counteracting the convective heating. They require more time to reach higher temperatures, where the mass loss rates are more significant, and hence the mixing of gaseous oxygen and hydrogen takes place further downstream, leading to longer flame fronts. The combination of the two models gives an intermediate result, and the addition of radiation does not seem to affect the flame length considerably.

A substantial difference between the two heat and mass transfer models is evident when examining the temperature of the discrete phase. This is plotted for models 1 and 3 in Fig. 4.18. In the Evaporation and Boiling model, the

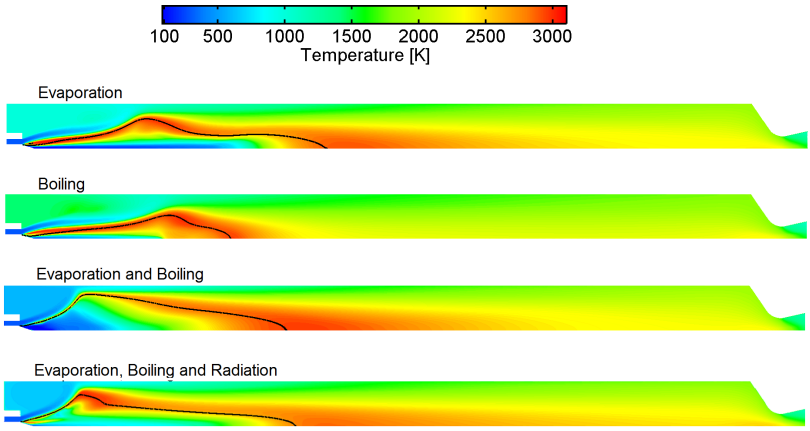

Figure 4.17.: Comparison of temperature field for the different heat transfer models

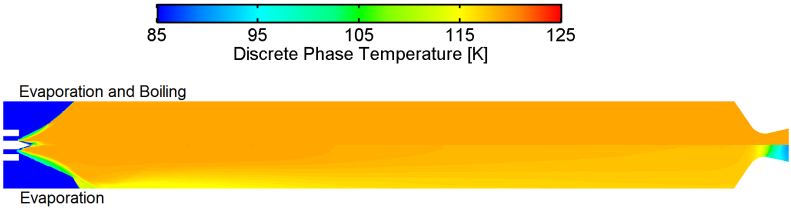

Figure 4.18.: Comparison of Discrete Phase temperature for the different heat transfer models

temperature of the discrete phase remains constant after the boiling has started and does not change since $\mathrm{d}T_p/\mathrm{d}t$ is zero in this case. Therefore the droplets cannot go back to the evaporation model after they have started boiling. In the pure evaporation case on the other hand, the temperature of the droplets does not remain constant but can change throughout the chamber. This is

especially dominant further downstream of the flame front, and in the nozzle. There, the particle temperature drops due to the interaction with the colder gas. The higher speeds leads to bigger Re_d and hence increased convective heat transfer and mass loss.

However, as seen in Fig. 4.19, close to 90 % of the discrete phase mass has already evaporated after the flame front and hence only a small number of droplets enters the nozzle and demonstrates this decrease in temperature. Fig. 4.19 illustrates the mass source over axial position for the four models, as well as the accumulated mass loss of the particles. It can be observed that the profiles of the Evaporation model and the Boiling model demonstrate an increase in the mass source at around 110 mm from the injector. This phenomenon is not present for the combined Evaporation and Boiling model.

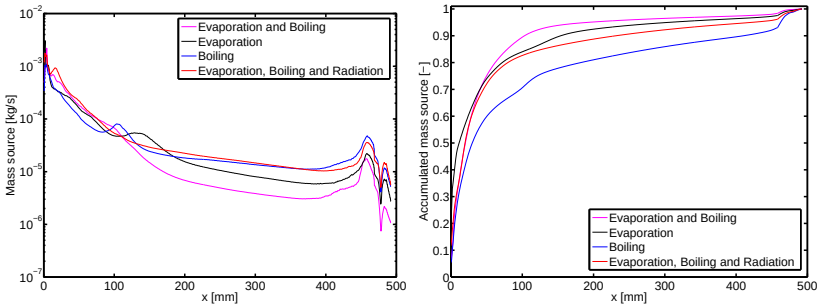

Figure 4.19.: Mass source over axial position (left) and accumulated evaporated mass over axial position (right) for the different heat transfer models

In order to understand the nature of this increase, the streamlines for the Evaporation model were compared to the ones of the Evaporation and Boiling one close to the flame front. This is plotted in Fig. 4.20. The Evaporation model shows a vortex in the vicinity of the flame bulge, which is accountable for the sudden mass loss increase at 110 mm. This vortex is present at the oxygen-rich side of the flame and can transfer heat from the flame front directly to the oxygen particles. This leads to their increased evaporation and to a higher mass

transfer. The oxygen expands after evaporation and serves as the driving force of the vortex. Similar is the behavior in the case of the pure Boiling model, which is not shown here, whereas the combined Evaporation and Boiling model shows no formation of a vortex in the flame front, but a laminar behavior instead (Fig. 4.20).

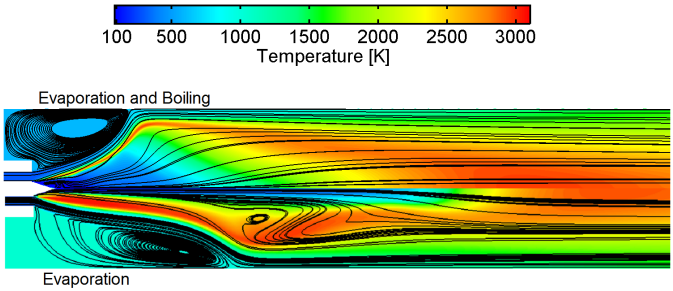

Figure 4.20.: Streamlines in the combustion zone for the Evaporation and the Evaporation/Boiling models

Apart from examining the summed mass source over axial position (Fig. 4.19), a more detailed insight into the particle trajectories can be given by viewing their diameter profile over the axial length of the chamber. For that reason, six diameter classes were chosen as shown in Fig. 4.21:

1. $(15 \pm 5)\ \mu$m
2. $(60 \pm 10)\ \mu$m
3. $(100 \pm 10)\ \mu$m
4. $(140 \pm 10)\ \mu$m
5. $(200 \pm 20)\ \mu$m
6. $(275 \pm 25)\ \mu$m

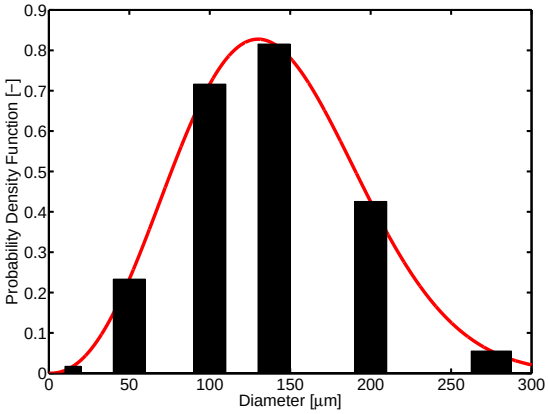

Figure 4.21.: Ranges in the Rosin-Rammler distribution used for the examination of the particles' diameter history

It is possible to track the trajectories of the droplets with initial diameters in one of these classes and examine how their diameter develops further downstream of the injection point. To illustrate this process, Fig. 4.22 is used. The diameter histories of particles in the Evaporation model with initial diameter (60 ± 10) μm are shown. The light blue lines represent the individual trajectories of several particles belonging to this class. Due to turbulent dispersion and different injection positions, not all particles follow the exact same trajectory. In fact although most particles seem to evaporate completely within the first 80 mm for this example, there are even some droplets that manage to reach 400 mm before vanishing. In order to characterize the diameter class as a whole and not as individual particles, the average diameter for each axial position was calculated, leading to the red line in the plot. In the following comparisons, only the average diameter is examined and no individual trajectories. It is important to note, that even if a single particle is present, which escapes the domain without completely evaporating, then the average diameter also seems to be bigger than zero for all axial positions, since it is built as the average of all particles. In order to avoid this problem, only particles that evaporate within $1.5\sigma_{st}$ of the average evaporation point are investigated for each class. σ_{st} represents the standard deviation.

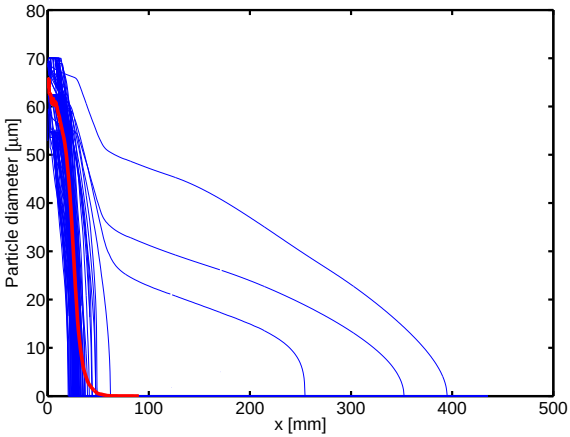

Figure 4.22.: Diameter history of particles with initial diameter (60 ± 10) μm in the Evaporation model

In the case of the Evaporation model, which has served as a reference so far, the particle trajectories for the six droplet classes are plotted in Fig. 4.23. As expected, smaller particles evaporate completely close to the injector. Droplets with higher initial diameters on the other hand seem to escape the domain without completely evaporating. As an example one can observe the diameter class with $d_0 = (275 \pm 25)\,\mu$m. The droplets escape the domain still in liquid form, and this is one of issues related to the Lagrange modeling. In reality, ligaments which are present in the combustion chamber take a long time to heat up but eventually break-up into smaller particles which evaporate locally, close to the injector. This secondary break-up is not modeled in the present work and hence larger droplets continue traveling until they exit through the nozzle. These larger droplets are in fact only a modeling assumption used to simulate the effect of the liquid ligaments and cannot realistically exist due to the Weber number of the A-10 case.

The average diameter at the exit of the nozzle is approximately 160 μm for this diameter class. This implies that close to 80 % of the droplets' mass has evap-

orated. So even if their diameter at the exit is non-negligible, a large fraction of their mass has already been transformed to gas. Furthermore, as Fig. 4.21 depicts, particles with high initial diameter represent only a small fraction of the total injected mass, and therefore the mass exiting the nozzle in liquid form is in fact negligible.

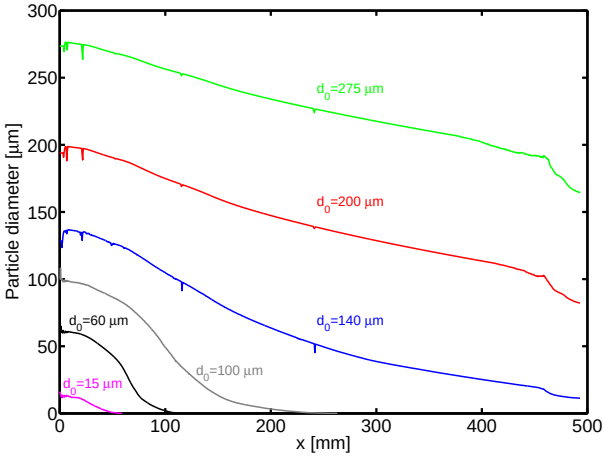

Figure 4.23.: Diameter history for the Evaporation model

A comparison between the separate models can be given in Fig. 4.24 for four different classes: (60 ± 10) μm, (140 ± 10) μm, (200 ± 20) μm and (275 ± 25) μm. One observes that the models including either only evaporation or only boiling, provide very similar results. Even for medium diameter classes like (140 ± 10) μm, the droplets seem to escape the domain without evaporating completely. A more realistic profile is provided by the combination of Evaporation and Boiling, which predicts that only particles with larger diameters leave through the nozzle. Including the radiation model as well, gives very similar results. The mass loss of the particles is however accelerated due to additional heat transfer mechanism and becomes significant especially for the larger diameters. In this case, even the droplets with (275 ± 25) μm initial diameter seem to evaporate completely. This is also represented when examining the

total mass source as shown in Table 4.6.

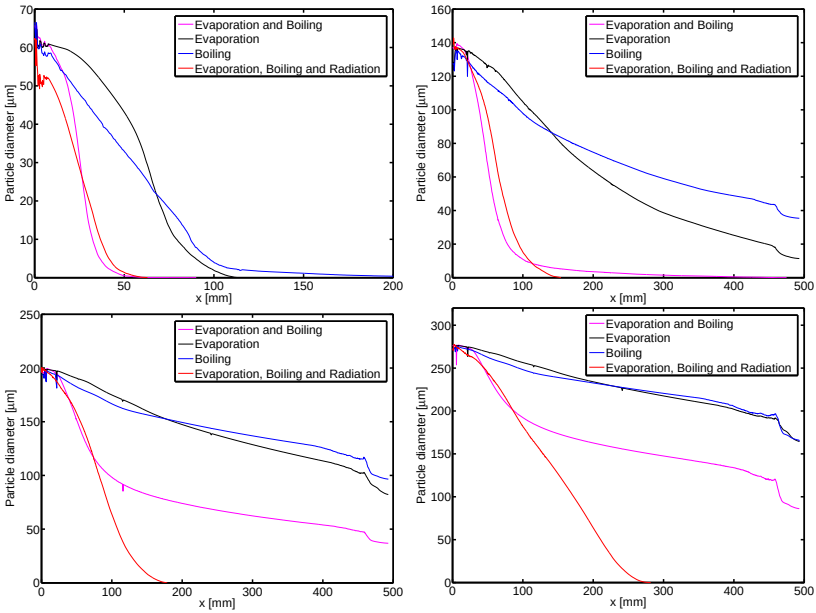

Figure 4.24.: Comparison of the particles' diameter history for different heat transfer models: (60 ± 10) μm, (140 ± 10) μm (top) and (200 ± 20) μm, (275 ± 25) μm (bottom)

The comparison of the models showed that the combination of evaporation and boiling leads to more realistic mass source distribution and droplet diameter profiles. Furthermore, it includes both surface and bulk mass transfer phenomena and is more complete from a physical point of view. Its ability to capture the physical processes in the single-element LOX/GH_2 chamber is also evident when examining the temperature profiles along axial direction and comparing them to the CARS measurements. This is done in Fig. 4.25. Even for radial positions close to the injector (y=0 mm, y=5 mm), the temperature profiles seem to adequately fit the experimental data and correctly predict the location of the flame front, i.e. the temperature maximum.

Table 4.6.: Maximal temperature and total mass source for the different heat and mass transfer models

Model description	Max. temperature	Mass source
Evaporation	2967.7 K	49.1 g/s
Boiling	3041.5 K	47.2 g/s
Evaporation & Boiling	3055.7 K	48.7 g/s
Evaporation, Boiling & Rad.	3007.7 K	49.5 g/s

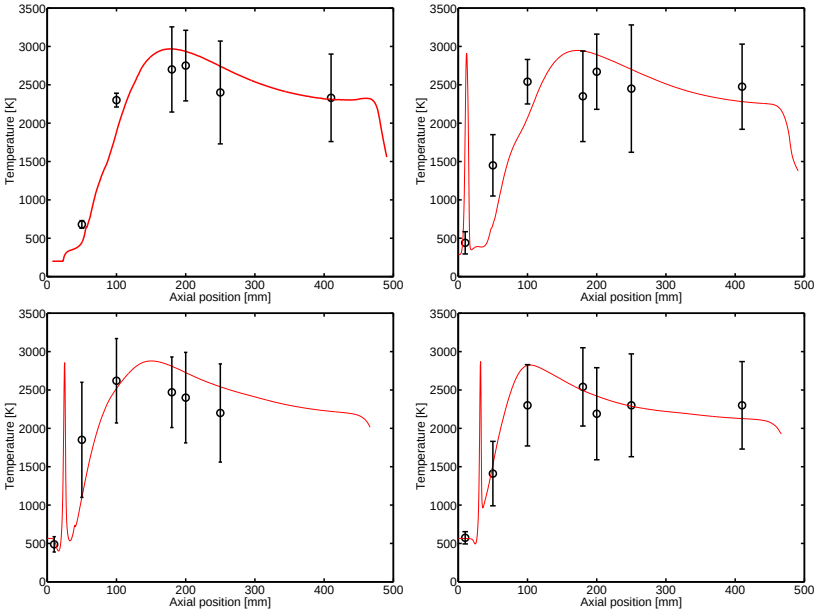

Figure 4.25.: Comparison of CARS temperature measurements with results of combined Evaporation and Boiling model at y=0 mm, y=5 mm (top) and y=10 mm, y=15 mm (bottom)

4.3.4. Effect of the droplet/wall interaction

Ideally, the liquid jet entering the combustion chamber is disintegrated into finer droplets (atomization), which upon interaction with the hot gas, evaporate completely near the injector. However, the results of the simulations carried out within the framework of this thesis show that several particles are able to propagate further downstream before completely evaporating. In the case that these droplets have a radial momentum component, their interaction with the chamber walls is inevitable.

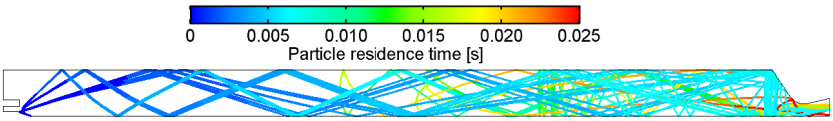

Figure 4.26.: Reflection of the particles on the wall

In the simulations carried out in the Sections 4.3.1, 4.3.2 and 4.3.3, a reflective boundary condition was applied. This however can lead to unrealistic results when examining the particle trajectories. An example of such trajectories is displayed in Fig. 4.26. Here the most extreme case of particles was chosen, since the figure illustrates the paths of the droplets with the highest diameter and biggest radial momentum, which leads to the longest residence duration. It can be observed that the droplets' properties remain unaltered, except for their velocity component normal to the wall, which changes direction upon collision with the chamber material.

To evaluate a different approach when modeling the wall boundary condition, the flashing model described in Section 4.2 was implemented. The temperature profile in the thrust chamber is illustrated in Fig. 4.27. It is evident from the high temperature values inside the recirculation zone, that a second reaction zone takes place close to the chamber walls. This is explained when considering that the droplets flashing directly on the walls produce significant amounts of oxygen vapor, which can in turn react with the hydrogen in the recirculation zone. This leads to the secondary combustion area and produces the high temperatures close to the faceplate.

Moreover, throughout the whole length of the combustion chamber, a high temperature boundary layer can be observed, as the zoom in Fig. 4.27 shows. The presence of oxygen close to the walls leads to a reactive boundary layer and hence a high temperature of the gases next to the wall.

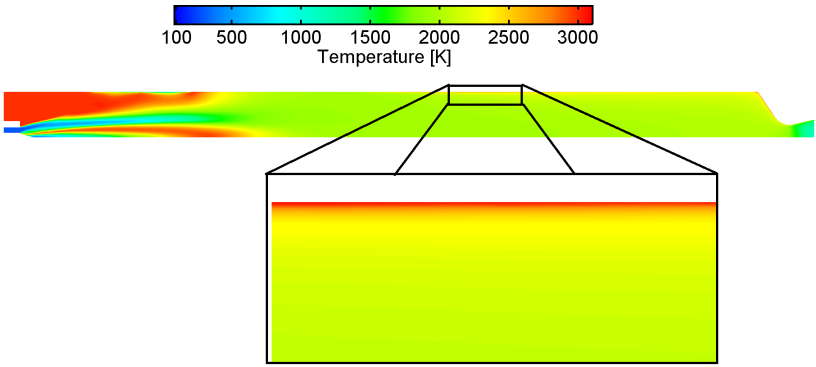

Figure 4.27.: Temperature plot for the flashing boundary condition

An examination of the OH^* and H_2O mass fractions in Fig. 4.28 validates this assumption. The presence of the hydroxyl radicals indicates the existence of a second flame front and the increased presence of water molecules represents the released products of the H_2/O_2 reaction.

The increased droplet evaporation at the collision locations is also understood when examining the mass source as a function of the axial location in Fig. 4.29 and Fig. 4.30. At the interaction locations of the droplets with the wall, an abrupt increase in evaporated mass is evident, leading to certain "spikes" as explicitly indicated by the arrows. Most of the particles which have not completely evaporated while in the combustion chamber, collide with the nozzle wall leading to a sudden rise in the mass source right before the nozzle entrance. Finally, a very small number of particles survives and enters the nozzle, which explains the unusually low mass source in the nozzle.

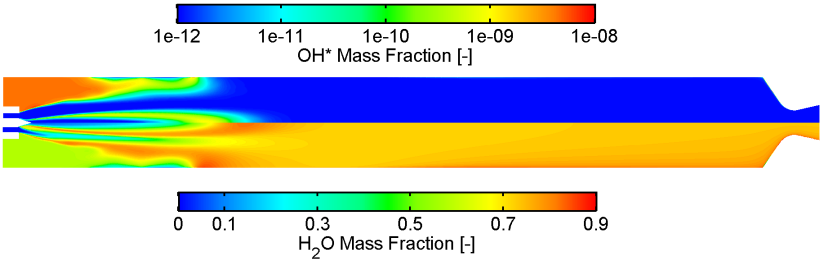

Figure 4.28.: OH^* and H_2O mass fraction in the thrust chamber in the case of flashing boundary condition

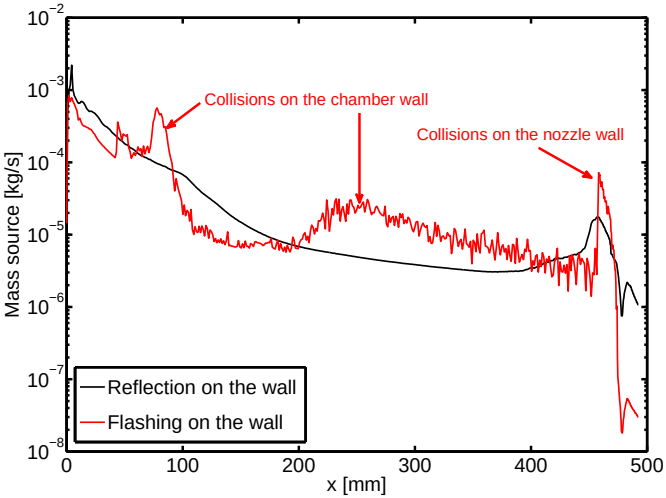

Figure 4.29.: Mass source over axial position for different wall boundary conditions

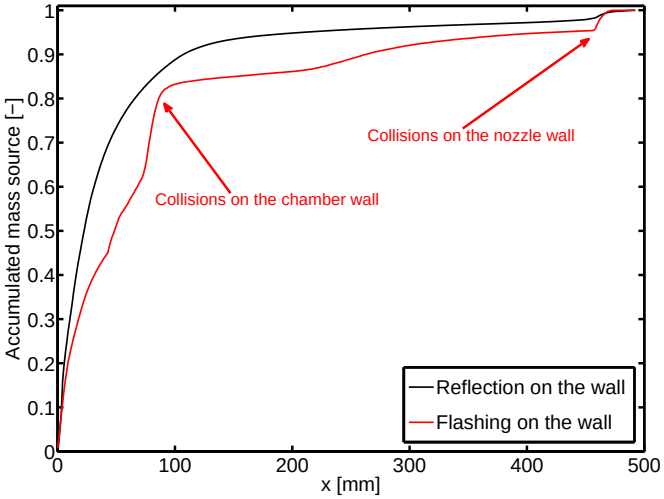

Figure 4.30.: Accumulated mass source over axial position for different wall boundary conditions

Although the flashing boundary condition could be used in certain conditions involving high chamber wall temperatures, it is not suitable for the simulation of the A-10 Mascotte case. The accumulated oxygen in the vicinity of the wall leads to an unphysical secondary reaction zone close to the faceplate, which does not coincide with the experimental data.

5. Conclusion and outlook

Within the frame of the present thesis, the cryogenic combustion of LOX and GH_2 was simulated for the A-10 Mascotte rocket combustor. The main purpose of the simulation was the examination of the Lagrange tracking module implemented in the commercial CFD code Fluent. According to this module, the liquid oxygen entering through the injector was modeled as a group of discrete particles able to exchange heat, mass and impulse with the gas phase. The calculations were carried out in a 2D axially symmetric domain and the Finite Volume Method was utilized for the solution of the RANS equations for the gas phase.

In order to initialize the simulation, a test case with gaseous oxygen injection was carried out in the absence of the Lagrange module, by using an Euler/Euler description. This first stable solution was used to initialize the temperature and mixture fraction fields for all subsequent simulations.

For the initial conditions of the liquid oxygen, a particle diameter distribution and an injection angle distribution were implemented as proposed by previous works describing the A-10 case's experimental and numerical results. The utilized Rosin-Rammler size distribution ensures a wide range of statistics and approximates the primary break-up of the liquid oxygen jet and ligaments, that cannot be directly simulated in RANS applications.

Although the droplet size distribution was preserved throughout the calculations in the thesis, a parameter study of the injection angle was performed. A uniform injection angle parallel to the chamber axis was found to match the OH^* measurements more effectively and was therefore implemented. However, the length of the flame was found to be unphysical since it reached up to the beginning of the nozzle, which was not expected in a single-element experimental combustor.

It was found that a reduction of the oxygen's injection velocity as well as a modification of the turbulent Schmidt and Prandtl numbers led to the wanted

effect of a shorter flame length. Upon comparison of the updated results with the CARS temperature measurements, a much better agreement was present. The liquid oxygen boundary conditions and settings of the turbulence model were therefore modified.

The main emphasis was then placed on the different heat and mass transfer models that can be included into the Lagrange tracking module. The effect of surface evaporation and bulk boiling on the droplets was examined. Both models resulted in plausible temperature fields but produced an inner vortex within the flame region, which was not expected. On the other hand a combination of the two models, with evaporation until the boiling temperature is reached and consequent boiling, demonstrated a more realistic behavior. In contrast to the separate evaporation and boiling models, it was found that fewer particles escape the domain through the nozzle without completely evaporating when the combined model is used. This fulfills the expectation that in reality, the majority of the particles should turn into vapor within the chamber and not exit the nozzle in liquid form. Also, apart from the temperature profile fitting very well with the CARS measurements, the absence of the aforementioned vortex in the reaction zone served as a validation that the combination of the two models approximates the reality more accurately. The extension of this model by including radiation modeling was also investigated. This provided very similar results with the model combining evaporation and boiling, was however also connected with high uncertainty of several modeling values like the emissivity and scattering factor of the droplets.

The Lagrange model includes a stochastic tracking to ensure sufficient statistics when modeling the liquid droplets. It was therefore observed that few particles with sufficient radial impulse component within the limits of the stochastic turbulence, were able to reach the chamber walls and undergo multiple reflections. To avoid these multiple reflections on the walls which are not realistic, an alternative wall boundary condition involving instantaneous flashing of the particles was examined. Unfortunately, this did not deliver the expected results since oxygen was accumulated close to the walls after the droplets' flashing and was able to interact with hydrogen leading to a second reaction zone close to the faceplate.

After an extensive examination of the A-10 Mascotte case with Fluent's Lagrange tracking module, the capabilites, strengths and weaknesses of the tool could be assessed. The modularity of the code enables the use of different initial

conditions, liquid phase properties and heat transfer models. After comparison of the provided models, numerical results approximating the experimental data to a sufficient degree were obtained. Unfortunately, the CARS measurements are subject to a high uncertainty indicating a high turbulence degree in the chamber, thereby not facilitating a comparison with CFD results. Also the OH^* emissions are restricted only to axial positions close to the injector, thereby not allowing a comparison of the flame length. The obtained results seem however plausible when considering typical flame profiles in O_2/H_2 rocket engines. On the downsides of the Lagrange module, the incapability of modeling large ligaments leads to some unrealistically large droplets being present in the chamber. Due to their high impulse- and heat-related inertia, they manage to escape the domain, which is not expected in a realistic rocket application. This could be avoided in the future by including a secondary break-up model in the simulations which would lead to a higher number of smaller droplets, able to easily evaporate locally. A special treatment of the wall boundary condition could also assist in this aspect, since it could enable a further break-down or film creation resulting from the larger diameters.

In order to investigate the A-10 test case in further detail, a 3D simulation would be interesting, since it would enable modeling of the corners in the rectangular chamber, which serve as larger recirculation zones, where the fraction of the oxygen droplets can be trapped. In addition, extending the modeling of the chemistry to a detailed finite rate reaction mechanism could induce further accuracy compared to the equilibrium chemistry, which is however sufficient for the fast reaction rates of O_2/H_2 combustion. Finally extending the Lagrange module to include other cryogenic propellants is necessary, to ensure that it can capture the effects related to other fuel combinations and thereby validate it generally for rocket engine applications.

A. Thermodynamic Properties of Oxygen

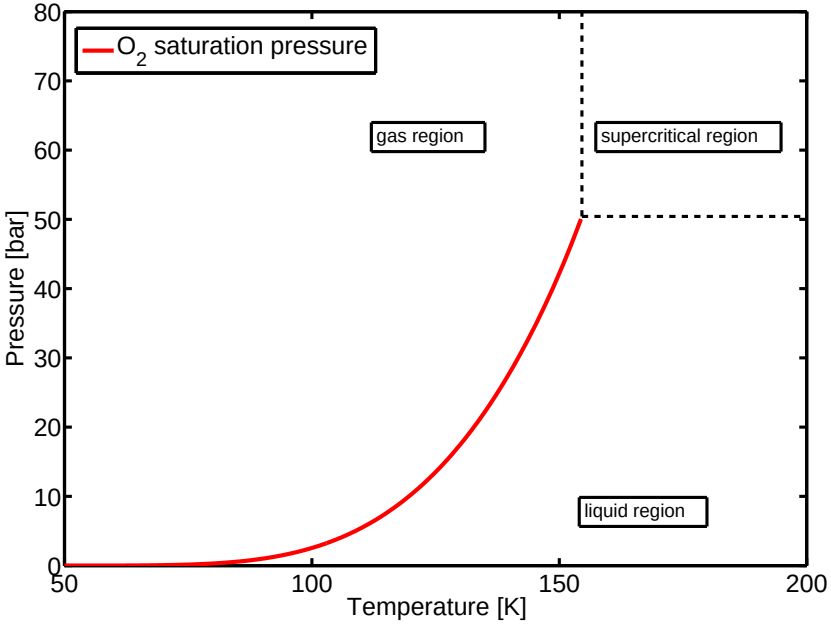

Figure A.1.: Saturation pressure of oxygen as a function of temperature

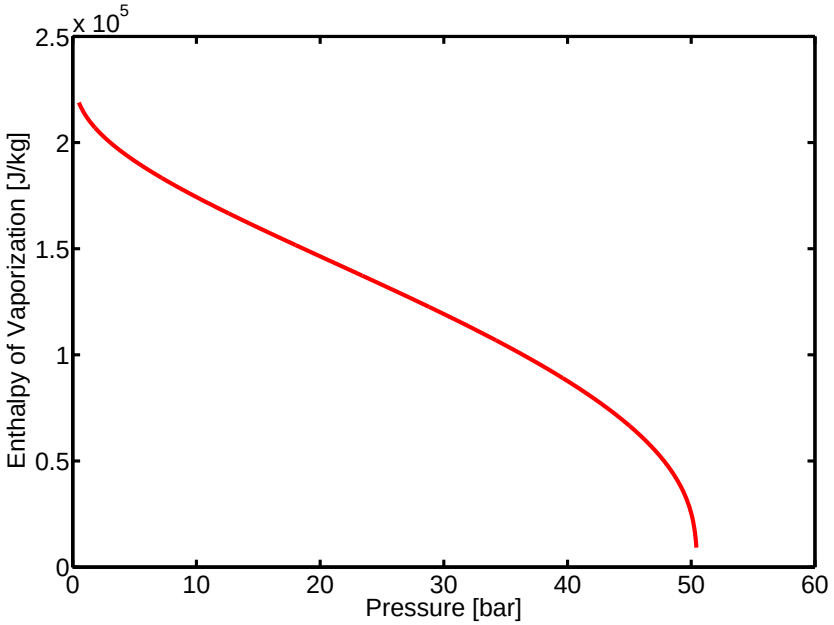

Figure A.2.: Enthalpy of vaporization of oxygen as a function of pressure

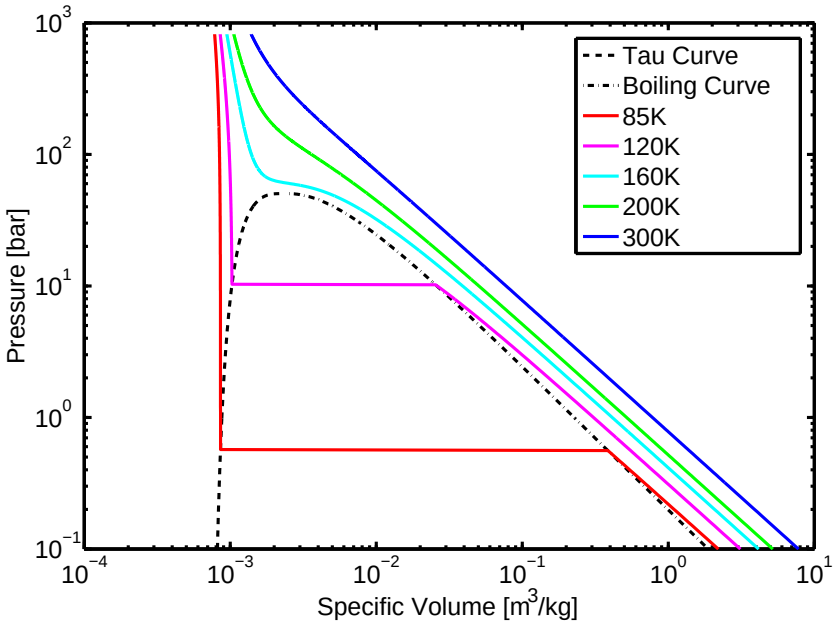

Figure A.3.: Pressure vs specific volume diagram of oxygen

B. Chapman-Enskog diffusion theory

The Chapman-Enskog model gives a prediction for the diffusion coefficient of two gas components as a function of the temperature and pressure. As already described in Eq. 2.29 [9], the diffusion coefficient is proportional to the temperature of the gases and drops inversely with the pressure.

Apart from the macroscopic quantities (T, p), the model requires knowledge of kinetic properties related to the Lenard-Jones potential of the gas components. The average collision diameter σ_C is given by

$$\sigma_C = \frac{\sigma_1 + \sigma_1}{2} \tag{B.1}$$

where σ_i represent the collision diameters of the respective gas molecules. The collision integral Ω is more complex and depends on the temperature and the energy of interaction ϵ_{12}, with

$$\epsilon_{12} = \sqrt{\epsilon_1 \epsilon_2} \tag{B.2}$$

The values for σ_i and ϵ_i are tabulated for most gases and the dependence of Ω on T and ϵ_{12} is shown in Fig. B.1, where k_B stands for the Boltzmann constant.

Using this models, the diffusion coefficient of oxygen into O_2, H_2O and H_2 was examined as a function of temperature for a constant pressure $p = 10\,\text{bar}$. This is illustrated in Fig. B.2.

The Enskog-Chapman model was used for the simulations in this thesis and its effect on the diffusion coefficient was examined for the case of the simulation 4 shown in Section 4.3.2 (v=2.18 m/s, $Pr_t = 0.90$ and $Sc_t = 0.60$, diffusion/convection based evaporation). The value of the diffusion coefficient within the chamber was calculated with the post-processor CFD-Post. Fig. B.3

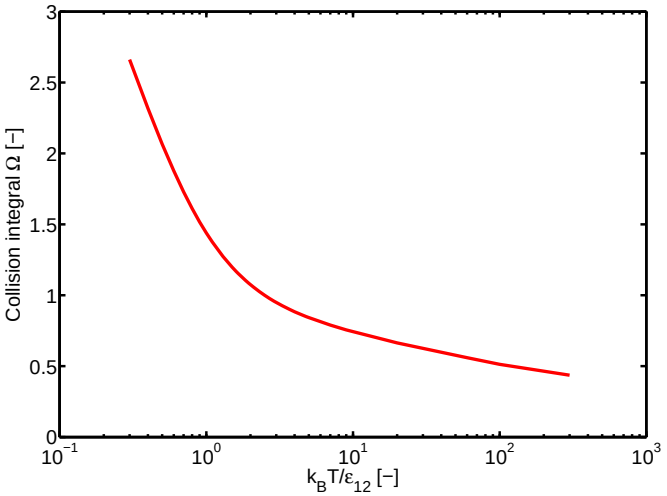

Figure B.1.: Dependence of the collision integral on temperature and interaction energy [9]

shows how this coefficient varies in different locations of the chamber. The average value along the axial position is plotted in Fig. B.4.

The average diffusion coefficient according to the Chapman-Enskog model remains almost constant throughout the combustion chamber and equal to $D = 2 \cdot 10^{-5}\,\mathrm{m}^2/\mathrm{s}$. It only starts increasing significantly in the nozzle, due to the lower pressure. However, the effect of the particles in the nozzle is negligible. For that reason, approximating the diffusion coefficient as a constant could theoretically provide very similar results as the more complex Chapman-Enskog model.

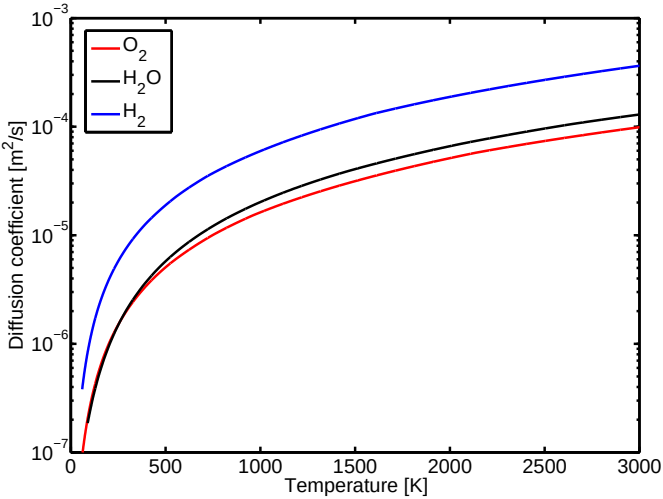

Figure B.2.: Dependence of diffusion coefficient on temperature

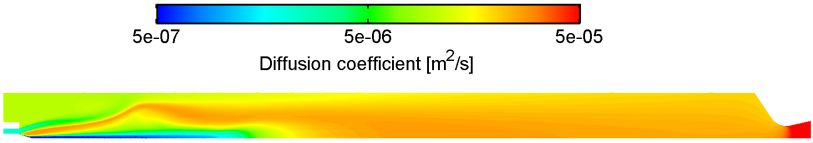

Figure B.3.: Diffusion coefficient in the combustion chamber

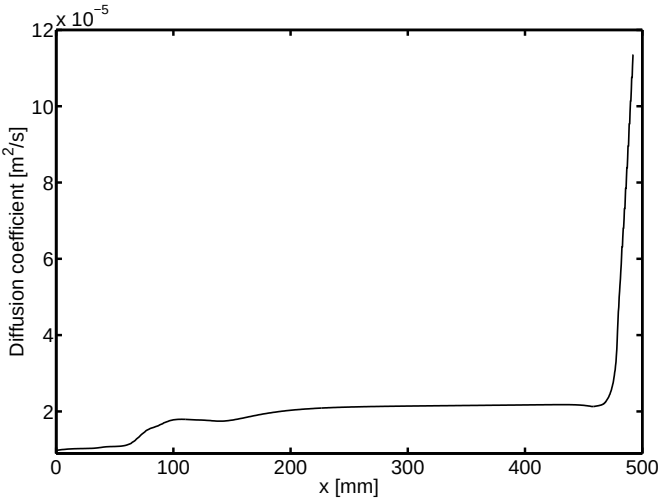

Figure B.4.: Average diffusion coefficient along axial position in the chamber

Bibliography

[1] ANSYS. ANSYS Fluent Theory Guide, release 16.0. 2015.

[2] Astrium. Vulcain 2 : Thrust chamber. Brochure, 2008.

[3] P. Atkins and J. De Paula. *Elements of physical chemistry*. Oxford University Press, USA, 2013.

[4] L. P. Bayvel and Z. Orzechowski. *Liquid atomization*. Washington, DC : Taylor & Francis, 1993.

[5] R. Begley, A. Harvey, and R. L. Byer. Coherent anti-stokes raman spectroscopy. *Applied Physics Letters*, 25(7):387–390, 1974.

[6] S. Candel, G. Herding, R. Synder, P. Scouflaire, C. Rolon, L. Vingert, M. Habiballah, F. Grisch, M. Pé, alat, et al. Experimental investigation of shear coaxial cryogenic jet flames. *Journal of Propulsion and Power*, 14(5):826–834, 1998.

[7] N. Chigier and Z. Farago. Morphological classification of disintegration of round liquid jets in a coaxial air stream. *Atomization and Sprays*, 2(2), 1992.

[8] H. Chiu and J. Oefeleinf. Modeling liquid-propellant spray combustion processes. *Liquid Rocket Thrust Chamber: Aspects of Modeling, Analysis, and Design, Progress in Aeronautics and Astronautics*, 200:251–293, 2004.

[9] E. L. Cussler. *Diffusion: mass transfer in fluid systems*. Cambridge university press, 2009.

[10] D. Daniel. Zwei- und dreidimensionale berechnung der strömung und verbrennung in einer h2/o2-raketenschubkammer. Diploma Thesis, 2012.

[11] O. Desjardins, J. McCaslin, M. Owkes, and P. Brady. Direct Numerical and Large-Eddy Simulation of primary atomization in complex geometries. *Atomization and Sprays*, 23(11), 2013.

[12] J. H. Ferziger and M. Peric. *Computational methods for fluid dynamics*. Springer Science & Business Media, 2012.

[13] T. Fiala and T. Sattelmayer. A posteriori computation of oh* radiation from numerical simulations in rocket combustion chambers. In *5th European Conference for Aeronautics and Space Sciences (EUCASS), Munich, July*, pages 1–5, 2013.

[14] P. Gerlinger. *Numerische Verbrennungssimulation: Effiziente numerische Simulation turbulenter Verbrennung*. Springer-Verlag, 2005.

[15] S. Gordon and B. J. McBride. Computer Program for Calculation of Complex Chemical Equilibrium Compositions, Rocket Performance, Incident and Reflected Shocks, and Chapman-Jouguet Detonations. *NASA*, 1976.

[16] W. Jones and J. Whitelaw. Calculation methods for reacting turbulent flows: a review. *Combustion and flame*, 48:1–26, 1982.

[17] F. Joos. *Technische Verbrennung*. Springer, 2006.

[18] O. Knab, M. Frey, J. Görgen, C. Maeding, K. Quering, and D. Wiedmann. Progress in combustion and heat transfer modelling in rocket thrust chamber applied engineering. *AIAA Paper*, 5477, 2009.

[19] K. K. Kuo. Principles of combustion. 1986.

[20] J. Lasheras, E. Villermaux, and E. Hopfinger. Break-up and atomization of a round water jet by a high-speed annular air jet. *Journal of Fluid Mechanics*, 357:351–379, 1998.

[21] A. Li and G. Ahmadi. Dispersion and deposition of spherical particles from point sources in a turbulent channel flow. *Aerosol science and technology*, 16(4):209–226, 1992.

[22] P. Mani. Numerical Analysis of the 10 bar MASCOTTE flow field. In O. J. Haidn, editor, *2nd International Workshop Rocket Combustion Modeling: Atomization, Combustion and Heat Transfer*. Deutsches Zentrum für Luft- und Raumfart, 2001.

[23] T. Ménard, S. Tanguy, and A. Berlemont. Coupling level set/VOF/ghost fluid methods: Validation and application to 3D simulation of the primary break-up of a liquid jet. *International Journal of Multiphase Flow*, 33(5):510–524, 2007.

[24] S. Morsi and A. Alexander. An investigation of particle trajectories in two-phase flow systems. *Journal of Fluid Mechanics*, 55(02):193–208, 1972.

[25] H. Ounis, G. Ahmadi, and J. B. McLaughlin. Brownian diffusion of submicrometer particles in the viscous sublayer. *Journal of Colloid and Interface Science*, 143(1):266–277, 1991.

[26] R. Parsley and Z. Baojiong. Thermodynamic power cycles for pump-fed liquid rocket engines. In Y. Vigor, H. Mohammed, H. James, and P. Michael, editors, *Liquid Rocket Thrust Chambers*, chapter 18, pages 621–648. American Institute of Aeronautics and Astronautics, 2004.

[27] N. Peters. *Turbulent combustion*. Cambridge university press, 2000.

[28] T. Poinsot and D. Veynante. *Theoretical and numerical combustion*. RT Edwards, Inc., 2005.

[29] M. Pourouchottamane, F. Dupoirieux, L. Vingert, M. Habiballah, and V. Burnley. Numerical analysis of the 10 bar mascotte flow field. Technical report, DTIC Document, 2001.

[30] P. Saffman. The lift on a small sphere in a slow shear flow. *Journal of fluid mechanics*, 22(02):385–400, 1965.

[31] SEFRAN. Space propulsion: Vulcain 2. Brochure, 2011.

[32] W. A. Sirignano. *Fluid dynamics and transport of droplets and sprays*. Cambridge University Press, 1999.

[33] K. D. Squires and J. K. Eaton. Preferential concentration of particles by turbulence. *Physics of Fluids A: Fluid Dynamics (1989-1993)*, 3(5):1169–1178, 1991.

[34] G. P. Sutton and O. Biblarz. *Rocket propulsion elements*. John Wiley & Sons, 2010.

[35] L. Vingert and M. Habiballah. Presentation of Test Case RCM 2: Cryogenic Spray Combustion at MASCOTTE. In O. J. Haidn, editor, *2nd International Workshop Rocket Combustion Modeling: Atomization, Combustion and Heat Transfer*. Deutsches Zentrum für Luft- und Raumfart, 2001.

[36] D. C. Wilcox et al. *Turbulence modeling for CFD*, volume 2. DCW industries La Canada, CA, 1998.

[37] F. Zheng. Thermophoresis of spherical and non-spherical particles: a review of theories and experiments. *Advances in colloid and interface science*, 97(1):255–278, 2002.

List of Tables

List of Figures